RTG Student Lecture: Measurement of CP violation in $B_s^0 \to \phi\phi$ decays at the LHCb experiment

Max Neuner (PI Heidelberg)

November 23 - December 7, 2015

1 Introduction to theoretical framework

This lecture covers the measurement of the CP-violating phase ϕ_s in $B_s^0 \to \phi\phi$ decays at the LHCb experiment. The following theoretical overview is taken from the book "Physics at the Terascale" [1], my diploma thesis [2] and the internal LHCb analysis note [3].

1.1 Flavour physics

The quark mass eigenstates $\mid q\rangle$ are not equal to the electroweak eigenstates $\mid q'\rangle$. They are constructed by rotating the mass eigenstates with the Cabbibo-Kobayashi-Maskawa(CKM) matrix V_{CKM}:

$$\begin{pmatrix} d' \\ s' \\ b' \end{pmatrix} = V_{CKM} \begin{pmatrix} d \\ s \\ b \end{pmatrix}, \tag{1}$$

$$V_{CKM} = \begin{pmatrix} V_{ud} & V_{us} & V_{ub} \\ V_{cd} & V_{cs} & V_{cb} \\ V_{td} & V_{ts} & V_{tb} \end{pmatrix}. \tag{2}$$

The weak interaction is the only fundamental force that can describe decays in which the flavour of the quarks is changed through the exchange of a $W^{\pm}$ boson in a charged current interaction with the Langrangian [1]

$$\mathcal{L}_{CC} = -\frac{g_2}{\sqrt{2}} \left(\overline{\tilde{u}}_L \gamma^\mu W_\mu^+ V_{CKM} \tilde{d}_L + \overline{\tilde{d}}_L \gamma^\mu W_\mu^- V_{CKM}^\dagger \tilde{u}_L \right). \tag{3}$$

Due to non-trivial off-diagonal elements, the V_{CKM} matrix allows inter-generational changes. The diagonal elements are close to 1 and the off-diagonals are small so that transitions within the same generation are strongly preferred. The complex CKM-matrix has 4 parameters: the three mixing angles θ_{12}, θ_{13} and θ_{23} and the phase δ.

Unitarity of the CKM-matrix $V_{CKM} V_{CKM}^\dagger = \mathbb{1}$ gives six equations for the off-diagonal elements that represent triangles in the complex plane, e.g.:

$$\frac{V_{us}V_{ub}^*}{V_{cs}V_{cb}^*} + \frac{V_{cs}V_{cb}^*}{V_{cs}V_{cb}^*} + \frac{V_{ts}V_{tb}^*}{V_{cs}V_{cb}^*} = 0. \tag{4}$$

The angles between two numbers in the complex plane can be computed as the argument of the division of the two. For this analysis, the angle β_s is relevant:

$$\beta_s \equiv arg\left(-\frac{V_{ts}V_{tb}^*}{V_{cs}V_{cb}^*}\right). \tag{5}$$

Using these angles and the flavour representation, the CKM matrix can be approximated by

$$V_{CKM} = \begin{pmatrix} |V_{ud}| & |V_{us}| & |V_{ub}|\, e^{-i\gamma} \\ -|V_{cd}| & |V_{cs}| & |V_{cb}| \\ |V_{td}|\, e^{-i\beta} & -|V_{ts}|\, e^{i\beta_s} & |V_{tb}| \end{pmatrix} + \mathcal{O}(\lambda^5), \tag{6}$$

where the elements V_{ub}, V_{td} and V_{ts} have a non-trivial imaginary part. These phases are responsible for CP violation. When the Lagrangian of the charged current interaction in Equation 3 is CP-transformed,

$$\mathcal{L}_{CC}^{CP} = -\frac{g_2}{\sqrt{2}}\left(\bar{\tilde{d}}_L\gamma^\mu W_\mu^- V_{CKM}\tilde{u}_L + \bar{\tilde{u}}_L\gamma^\mu W_\mu^+ V_{CKM}^\dagger \tilde{d}_L\right), \tag{7}$$

one can see that CP is broken if $V_{CKM} \neq V_{CKM}^*$, i.e. the phase is not zero. This is also illustrated in the $b \to u$ sketch shown in Fig. 1. The $b \to u$ and CP-transformed $\overline{b} \to \overline{u}$ couplings that are given by V_{ub} and V_{ub}^* are different for a non-trivial complex phase. It is the only way that CP-violation can be introduced in the quark sector of the SM.

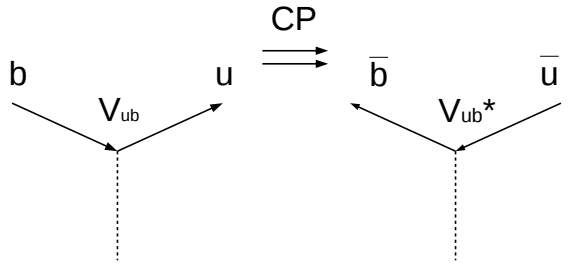

Figure 1: $b \to u$ and CP-transformed $\overline{b} \to \overline{u}$ transition in the Standard Model

1.2 Measurement of complex phase differences

Consider a single amplitude $A = |A|\, e^{i\phi}$. When taking the absolute square $A^*A = |A|^2\, e^{i(\phi-\phi)} = |A|^2$ the phase cannot be observed. For decay amplitudes describing a decay of e.g. a B-meson to a final state f, $B \to f$, the phase consists of a weak phase ϕ

introduced from the coupling constants that changes sign under CP transformation $\bar{B} \to \bar{f}$ and a strong phase δ that does not change sign and originates from strong CP-conserving processes:

$$\begin{aligned} A &= |A|\, e^{i(\phi+\delta)}, \\ \bar{A} &= |A|\, e^{i(-\phi+\delta)}. \end{aligned} \tag{8}$$

For the sum of single amplitudes $A = A_1 + A_2$, the phase is still present in the interference terms

$$\begin{aligned} |A|^2 &= |A_1 + A_2|^2 \\ &= |A_1|^2 + |A_2|^2 + |A_1 A_2|\, (e^{i((\phi_1+\delta_1)-(\phi_2+\delta_2))} + e^{i((-\phi_1-\delta_1)+(\phi_2+\delta_2))}) \\ &= |A_1|^2 + |A_2|^2 + 2\,|A_1 A_2| \cos(\Delta\phi + \Delta\delta) \end{aligned} \tag{9}$$

and the CP-transformed amplitude $\bar{A}$ is computed as

$$\begin{aligned} \left|\bar{A}\right|^2 &= \left|\bar{A}_1 + \bar{A}_2\right|^2 \\ &= |A_1|^2 + |A_2|^2 + |A_1 A_2|\, (e^{i((-\phi_1+\delta_1)-(-\phi_2+\delta_2))} + e^{i(-(-\phi_1+\delta_1)+(-\phi_2+\delta_2))}) \\ &= |A_1|^2 + |A_2|^2 + 2\,|A_1 A_2| \cos(-\Delta\phi + \Delta\delta). \end{aligned} \tag{10}$$

Note that, whereas the phases depend on the choice of convention, the phase difference is an observable quantity. Additionally, note that due to the even cosine function the strong phase difference is needed to measure the weak phase difference. Thus, CP-violation can only be measured in the interference of two amplitudes when there are two phases of which one flips sign under CP transformation. The weak phases are related to the phases of the CKM matrix elements. An example for direct CP violation is given by the decays $B^0 \to K^+\pi^-$ and $\bar{B}^0 \to K^-\pi^+$ where the tree amplitude in Fig. 2 (left) interferes with the loop-induced Penguin amplitude in Fig. 2 (right) that involve different CKM elements. However, the hadronic strong phases are really notoriously hard to calculate in Penguin diagrams and therefore, the result is difficult to interpret in terms of CKM angles.

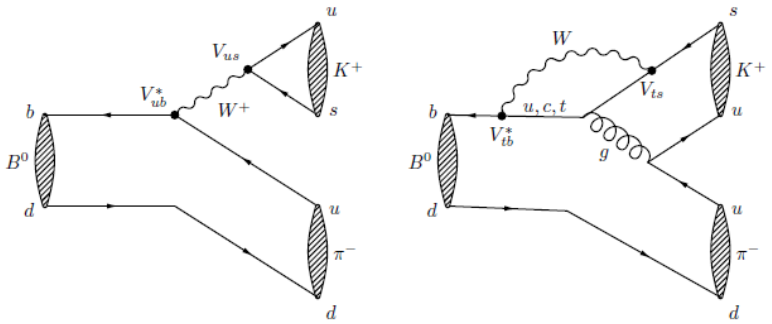

Figure 2: Tree-level(left) and Penguin(right) Feynman diagram of the decay $B^0 \to K^+\,\pi^-$

1.3 Flavour-changing neutral currents

Inter-generational quark transitions without charge exchange are called flavour-changing neutral currents (FCNC). Since these are not allowed on tree level, this process is only possible via a loop diagram shown in Fig. 3 a) in which a $W^{\pm}$ boson and an up-type quark are exchanged.

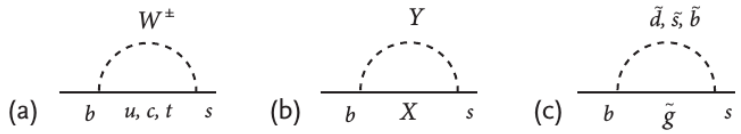

Figure 3: the skeleton $b \to s$ transition in (a) the Standard Model; (b) with generic new physics and (c) a possible MSSM amplitude with gluinos and squarks; taken from [1]

The Standard Model amplitude $\mathcal{A}$ for a $b \to s$ transition is the sum of all possible quark flavours in the loop, but due to the high top mass it is dominated by the top quark.

The study of FCNC processes is very interesting because they are suppressed in the SM. Since the particles in the loop are created virtually, new particles can contribute to the loop diagrams that are much heavier than the b energy scale. Note that the SM top is already much heavier. Fig. 3 b) and c) show Beyond-the-Standard-model (BSM) processes that might compete with the small Standard Model background. However, when they really exist, these contributions A_N must be tiny compared to the overwhelming SM amplitude A_{SM}. Though, in the absolute square of the total amplitude

$$A = |A_{SM} + A_N| = |A_{SM}|^2 + A_{SM}A_N^* + A_{SM}^* A_N + |A_N|^2 \tag{11}$$

the new contributions A_N appear in the interference terms that are sensitive to phase differences in the amplitudes. For this reason, phase differences are especially sensitive to New Physics contributions.

1.4 Mixing of neutral B-mesons

Meson mixing describes the possible transitions from one meson flavour state to the other via a flavour-changing neutral current (FCNC) shown in Fig. 4 for the B_s^0 in which W-bosons are exchanged.[1]

The time-development of the initially-produced flavour states $|\, B_s^0\rangle$ and $|\, \bar{B}_s^0\rangle$ can be computed with a phenomenological time-dependent Schrödinger equation:

$$-\frac{\partial}{\partial t}\begin{pmatrix} |\, B_s^0\rangle \\ |\, \bar{B}_s^0\rangle \end{pmatrix} = \left(\mathbf{M} - \tfrac{\mathbf{i}}{\mathbf{2}}\mathbf{\Gamma}\right)\begin{pmatrix} |\, B_s^0\rangle \\ |\, \bar{B}_s^0\rangle \end{pmatrix} \tag{12}$$

[1]The contributions from Penguin diagrams are neglected.

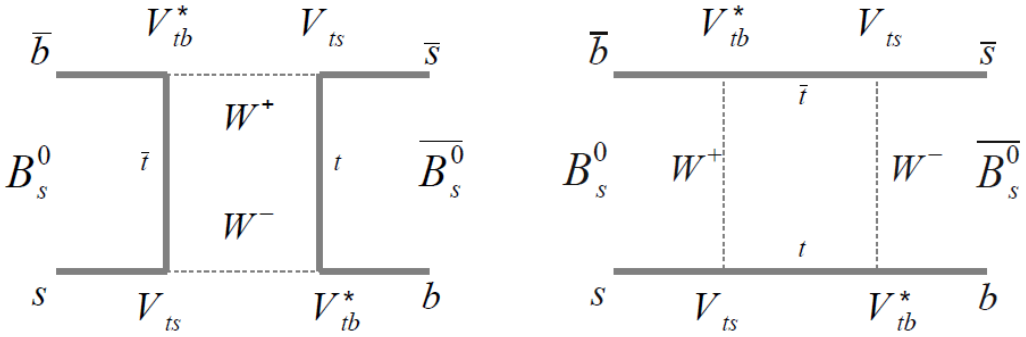

Figure 4: B_s^0 mixing diagrams in the Standard Model

with the the mass matrix $\mathbf{M}$ and the decay matrix $\mathbf{\Gamma}$ in the Hamiltonian. The diagonal elements are the masses $M_{L/H}$ and the decay widths $\Gamma_{L/H}$ so that the mass states $\mid B_L\rangle = p \mid B_s^0\rangle + q \mid \bar{B}_s^0\rangle$ and $\mid B_H\rangle = p \mid B_s^0\rangle - q \mid \bar{B}_s^0\rangle$ develop in time with

$$\begin{aligned} \mid B_L\rangle(t) &= e^{-iM_L t} e^{-\frac{\Gamma_L}{2}t} \mid B_L\rangle \\ \mid B_H\rangle(t) &= e^{-iM_H t} e^{-\frac{\Gamma_H}{2}t} \mid B_H\rangle \end{aligned}$$

and the flavour states can be written as

$$\begin{aligned} \mid B_s^0\rangle(t) &= \frac{1}{2p}\left(e^{-iM_L t} e^{-\frac{\Gamma_L}{2}t} \mid B_L\rangle + e^{-iM_H t} e^{-\frac{\Gamma_H}{2}t} \mid B_H\rangle\right) \\ \mid \bar{B}_s^0\rangle(t) &= \frac{1}{2q}\left(e^{-iM_L t} e^{-\frac{\Gamma_L}{2}t} \mid B_L\rangle - e^{-iM_H t} e^{-\frac{\Gamma_H}{2}t} \mid B_H\rangle\right). \end{aligned} \tag{13}$$

Inserting the mass eigenstates, the amplitude to observe an initially-produced B_s^0 in the same flavour (in the un-mixed state) at time t is

$$\begin{aligned} \langle B_s^0 \mid B_s^0(t)\rangle &= e^{-i(m_s - i\frac{\Gamma_s}{2})t}\left[\cosh\frac{\Delta\Gamma_s t}{4}\cos\frac{\Delta m_s t}{2} - i\sinh\frac{\Delta\Gamma_s t}{4} sin\frac{\Delta m_s t}{2}\right] \\ &\overset{\Delta\Gamma_s << \Gamma}{\approx} e^{-i(m_s - i\frac{\Gamma_s}{2})t}\ \cos\frac{\Delta m_s t}{2} \end{aligned} \tag{14}$$

and the amplitude that it is in the mixed state is

$$\begin{aligned} \langle \bar{B}_s^0 \mid B_s^0(t)\rangle &= e^{-i(m_s - i\frac{\Gamma_s}{2})t}\ \frac{q}{p}\left[-\sinh\frac{\Delta\Gamma_s t}{4}\cos\frac{\Delta m_s t}{2} - i\cosh\frac{\Delta\Gamma_s t}{4} sin\frac{\Delta m_s t}{2}\right] \\ &\overset{\Delta\Gamma_s << \Gamma}{\approx} e^{-i(m_s - i\frac{\Gamma_s}{2})t}\ \frac{q}{p}\ i\sin\frac{\Delta m_s t}{2}. \end{aligned} \tag{15}$$

This is the reason why Δm_s is also called the mixing frequency. Comparing this with the conjugate mixing process

$$\langle B_s^0 \mid \bar{B}_s^0(t)\rangle \overset{\Delta\Gamma_s << \Gamma}{\approx} e^{-i(m_s - i\frac{\Gamma_s}{2})t}\ \frac{p}{q}\ i\sin\frac{\Delta m_s t}{2}, \tag{16}$$

the ratio p/q flips and its phase is related to the weak phase from the CKM matrix elements that changes sign whereas the strong phase is given by $i = e^{i\pi/2}$.

1.5 CP-violation

There are three different types of CP-violation that can, however, occur at the same time.

- **Direct CP violation**, often called CP violation in decay, appears when the decay rates of the CP-conjugate processes $\Gamma(X \to f)$ and $\Gamma(\bar{X} \to \bar{f})$ with particle X and final CP-eigenstate f are not equal. An example was already given by the decays $B^0 \to K^+\pi^-$ and $\bar{B}^0 \to K^-\pi^+$ where the strong phase difference of the hadronic processes of the Penguin diagram cannot be calculated.

- **CP violation in mixing** of neutral mesons X^0 and $\bar{X}^0$ is related to different transition probabilities $\mathcal{P}(X^0 \to \bar{X}^0)$ and $\mathcal{P}(\bar{X}^0 \to X^0)$ which leads to an excess of particles of one flavour when assuming no direct CP violation but equal X^0-$\bar{X}^0$ production. In this case, as discussed in the previous section, the strong phase difference between the two mixing processes $X^0 \to \bar{X}^0$ and $\bar{X}^0 \to X^0$ is exactly $\pi/2$ whereas the strong phase in a sub-sequent decay is the same for $B_s^0 \to f$ and $\bar{B}_s^0 \to \bar{f}$ by definition. For one single dominant decay amplitude, this allows a very clean determination of the weak phases. For example, the time-integrated asymmetry a_{SL}^d is measured in semi-leptonic decays $B^0 \to X\mu\nu$ which was presented by Lucia last year. However, the tiny SM expectation of the asymmetry makes the analysis challenging.

- **CP violation through interference** between the decay and the decay after mixing can only occur when a final CP eigenstate f_{CP} can be reached in the decay of X^0 and $\bar{X}^0$. Thereby, the amplitudes where X^0 directly decays into the final state, $X^0 \to f_{CP}$, and where it first mixes into $\bar{X}^0$, $X^0 \to \bar{X}^0 \to f_{CP}$, interfere as it is illustrated for the B_s^0 meson in Fig. 5.

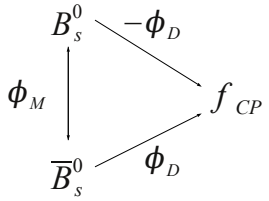

Figure 5: Illustration of CP violation in interference between the direct decay $B_s^0 \to f_{CP}$, and the decay after mixing, $B_s^0 \to \bar{B}_s^0 \to f_{CP}$

This kind of CP violation was discovered in the B-system in the decay $B^0 \to J/\Psi K_s^0$. Again, the strong mixing phase is given by $\pi/2$, the weak phase ϕ_M for B_s^0 mixing depends on the CKM matrix elements V_{ts} and V_{tb}

$$\phi_M = -2\arg(V_{ts}V_{tb}^*) \tag{17}$$

and the decay phase ϕ_D is decay-specific. Both phases ϕ_M and ϕ_D depend on the convention of the CKM matrix but the phase difference $\phi_s = \phi_M - 2\phi_D$ is an observable quantity.

1.5.1 Time-dependent decay rate into a final state $B_s^0 \to f$

When the B_s^0 decays into a final state f, the time-dependent decay rate $\frac{d\Gamma(B_s^0 \to f)}{dtN_f}$ is the absolute square of the transition amplitude:

$$\frac{d\Gamma(B_s^0 \to f)}{dtN_f} \;=\; \left|\langle f \mid B_s^0\rangle\right|^2 . \tag{18}$$

that are given for the decay rates of B_s^0 and $\bar{B}_s^0$ by

$$\frac{d\Gamma(B_s^0 \to f)}{dtN_f} \;=\; |A_f|^2 \; e^{-\Gamma_s t}\left\{\frac{1+|\lambda_f|^2}{2}\;\cosh\frac{\Delta\Gamma_s t}{2} \;+\; \frac{1-|\lambda_f|^2}{2}\;\cos(\Delta m_s t)\right.$$
$$\left. -Re\lambda_f \;\sinh\frac{\Delta\Gamma_s t}{2} - Im\lambda_f \;\sin(\Delta m_s t)\right\} \tag{19}$$

and

$$\frac{d\Gamma(\bar{B}_s^0 \to f)}{dtN_f} \;=\; |A_f|^2\,\frac{1}{1-a}\; e^{-\Gamma_s t}\left\{\frac{1+|\lambda_f|^2}{2}\;\cosh\frac{\Delta\Gamma_s t}{2} \;-\; \frac{1-|\lambda_f|^2}{2}\;\cos(\Delta m_s t)\right.$$
$$\left. -Re\lambda_f \;\sinh\frac{\Delta\Gamma_s t}{2} + Im\lambda_f \;\sin(\Delta m_s t)\right\}, \tag{20}$$

where $\lambda_f = (q/p)(\bar{A}_f/A_f) = -\eta_{CP} e^{i(-\phi_M + 2\phi_D)}$ with the decay amplitudes $A_f = A(B_s^0 \to f)$ and $\bar{A}_f = A(\bar{B}_s^0 \to f)$, $a = 1 - |q/p|^2$ and N_f is a time-dependent normalisation factor. The difference between the two decay rates is introduced by a non-trivial imaginary part of the CP-violation parameter $Im(\lambda_f) \neq 0$. The decay rates are basically exponential decay functions that are modulated by the mixing oscillation with the tiny amplitude $Im(\lambda_f) \neq 0$ and the frequency Δm_s as shown in simulated events in Fig. 6. For visibility, the SM expectation amplitude is enlarged by a factor of 10.

1.6 CP-violating phase ϕ_s in the decay $B_s^0 \to J/\Psi\,\phi$ and $J/\Psi\,\pi^+\pi^-$

In the tree level diagram in Fig. 7 of the decay $B_s^0 \to J/\Psi\;\phi(\to KK)\;(or)\;J/\Psi\pi^+\pi^-$, the $\bar{b}$-quark of the B_s^0 meson decays into a $\bar{c}$-quark by emitting a W^+ boson. While the $\bar{c}$-quark hadronises to become a J/Ψ, the s - $\bar{s}$ final state forms a ϕ meson or an $f_{0/2}$ resonance that can decay into two pions.

Neglecting higher-order Penguin diagrams, the decay amplitude A_f is proportional to the CKM matrix elements V_{cs} and V_{cb}^* that do not have a complex phase in the parameterisation, i.e. the observable CP-violating phase difference $\phi_s = \phi_M - 2\phi_D =$

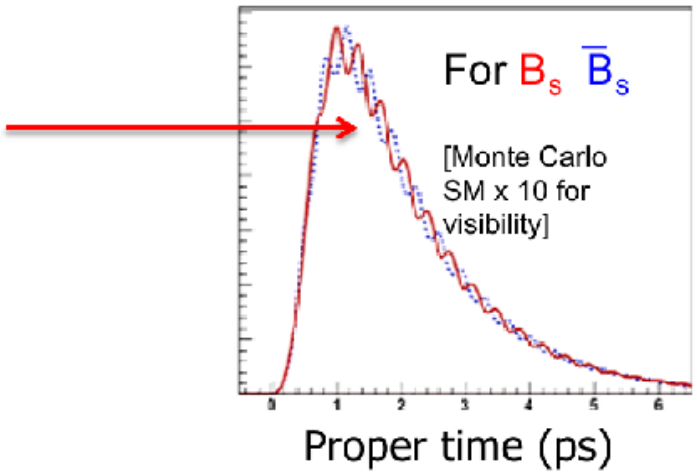

Figure 6: Simulated $B_s^0/\bar{B}_s^0$ decay time distribution with mixing. The SM expectation amplitude is enlarged by a factor of 10 for visibility.

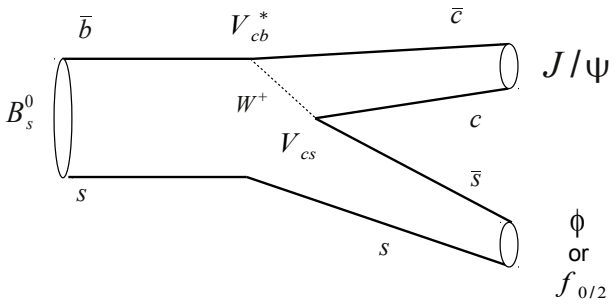

Figure 7: Tree level Feynman diagram of the decay $B_s^0 \to J/\Psi\ \phi\ or\ f_0/f_2(\to \pi^+\pi^-)$

$2\ arg(V_{ts}^* V_{tb}) - 2\ arg(V_{cb} V_{cs}^*)$ is equal to $-2\beta_s$. Note that while the phases ϕ_M and ϕ_D are only chosen relative to each other, ϕ_s is a measurable physical quantity.

In recent measurements at LHCb [4] and [5], the phase ϕ_s has been measured to be ϕ_s = -0.058 $\pm$ 0.049 $\pm$ 0.006 rad in the J/Ψ ϕ mode and ϕ_s = 0.070 $\pm$ 0.068 $\pm$ 0.008 rad in the J/Ψ $\pi^+\pi^-$ mode which is compatible with the Standard Model expectation value of ϕ_s = -0.0363 $\pm$ 0.0013 rad. In Fig. 8, the invariant $\mu^+\mu^- K^+ K^-$ mass distribution from 2011 and 2012 data at LHCb is shown with a clean signal peak of about 100000 events.

It is the goal of the coming years to further improve the statistical sensitivity of the ϕ_s measurement and put more stringent limits on possible new effects.

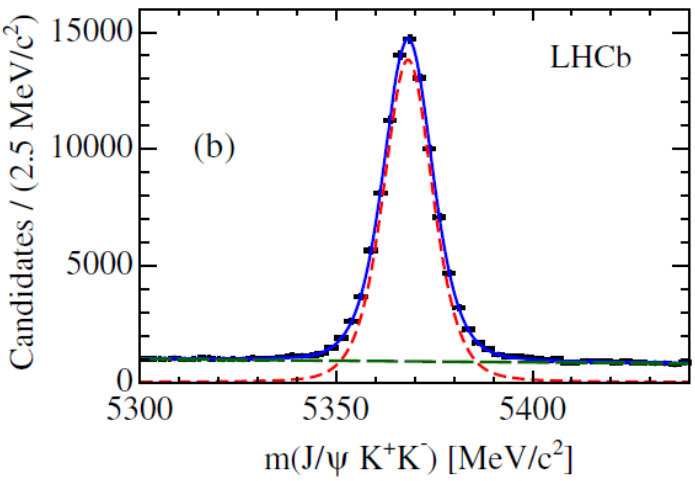

Figure 8: Invariant $\mu^+\mu^- K^+K^-$ mass distribution from 2011 and 2012 data at LHCb.

1.7 Time-dependent decay rate for $B_s^0 \to \phi\phi$

In parallel, channels which are sensitive to ϕ_s but which at the same time offer a different dependence on New Physics through additional quantum loops, are investigated. One such a channel is the Penguin $B_s^0 \to \phi\phi$. In principle, this analysis is similar to the above-mentioned ones and consists of a time-dependent analysis of P-violation in the interference between mixing and decay where the B_s^0 mixing is identical for both decays. The large difference between the two decays is provoked by the different Feynman decay diagrams. Unlike in $J/\Psi\phi$, where the decay products are mainly produced in a tree Feynman diagram, the decay $B_s^0 \to \phi\phi$ can only proceed via a rare penguin process, a loop diagram that is given in Fig. 9.

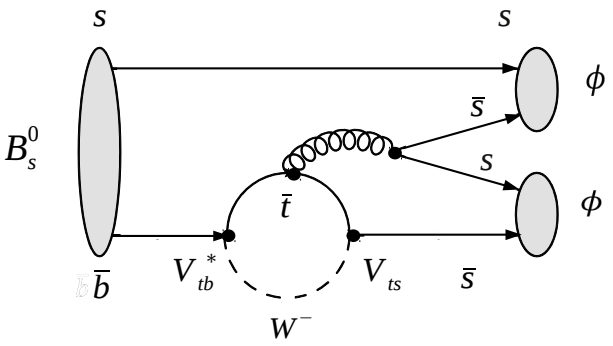

Figure 9: Feynman diagram of the decay $B_s^0 \to \phi\phi$

Thus, this decay channel is not only sensitive to New Physics contributions in mixing, but additionally to possible new effects in the quantum corrections of the loop-suppressed

decay amplitude that is mediated via a gluon providing a different operator to test. Therefore, the observed CP-violating phase $\phi_{s,(\phi\phi)}$ differs from $\phi_{s,(J/\Psi\phi)}$ and is sensitive to the presence of additional new phenomena as it is sketched in Fig. 10.

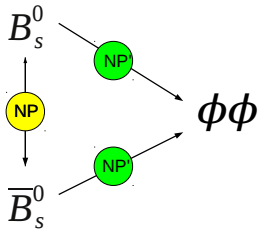

Figure 10: Illustration of CP violation in interference between the direct decay $B_s^0 \to \phi\phi$, and the decay after mixing, $B_s^0 \to \bar{B}_s^0 \to \phi\phi$ with possible New Physics contribution

Considering the CKM matrix elements for this decay, the weak phase ϕ_D is related as $\phi_D = \arg(V_{tb}^* V_{ts})$ which are exactly the same elements present in the mixing diagram in Fig. 4. For this reason, the Standard Model expectation value for the CP-violating phase $\phi_{s,(\phi\phi)}$, further simply denoted as ϕ_s, vanishes:

$$\phi_s = \phi_M - 2\phi_D = 0. \tag{21}$$

Any significant observed CP-violation would indicate the existence of new particles and couplings.

2 The LHCb experiment

In order to study the decay $B_s^0 \to \phi\phi$, a large number of B_s^0 mesons is needed. At the Large Hadron Collider (LHC), they are produced numerously in proton-proton collisions due to a large $b\bar{b}$ cross section with a beam energy of 7/8/13 TeV. The LHCb detector, located at one of the interaction points, has the excellent vertex and momentum resolution that is needed to study the rapidly oscillating B_s^0 mesons.

The LHCb experiment is designed to study heavy flavour physics at the LHC. In contrast to the larger experiments ATLAS and CMS, LHCb is operated at a lower luminosity of $\mathcal{L} = 2 \cdot 10^{32} cm^{-2} s^{-1}$ by separating the colliding beams. The advantage of a lower interaction rate is to have only one or two proton-proton interactions per bunch crossing which simplifies the association of the primary vertices. Additionally, the occupancy in the detector is lower which reduces combinatorial background. Nevertheless, a number of 10^{12} $b\bar{b}$ pairs are produced in 10^7 seconds that can be reached in a year of data taking. Due to the high center of mass energy of the protons, the B-hadrons are predominantly produced in the forward and backward direction as it is shown in Fig. 11.

This is the reason why LHCb is built as a single-arm forward spectrometer. The angular coverage ranges within the pseudorapidity η of approximately $1.6 < \eta < 4.9$ [6]. A schematic illustration of the side view of the LHCb-detector is shown in Fig. 12 that is taken from [6].

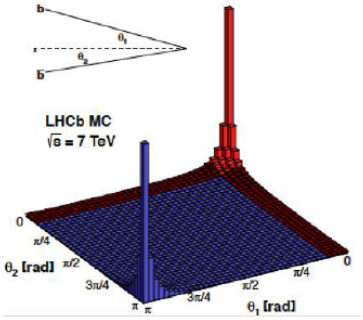

Figure 11: Number of produced B mesons as function of the polar angles $\theta_{1/2}$ in arbitrary units.

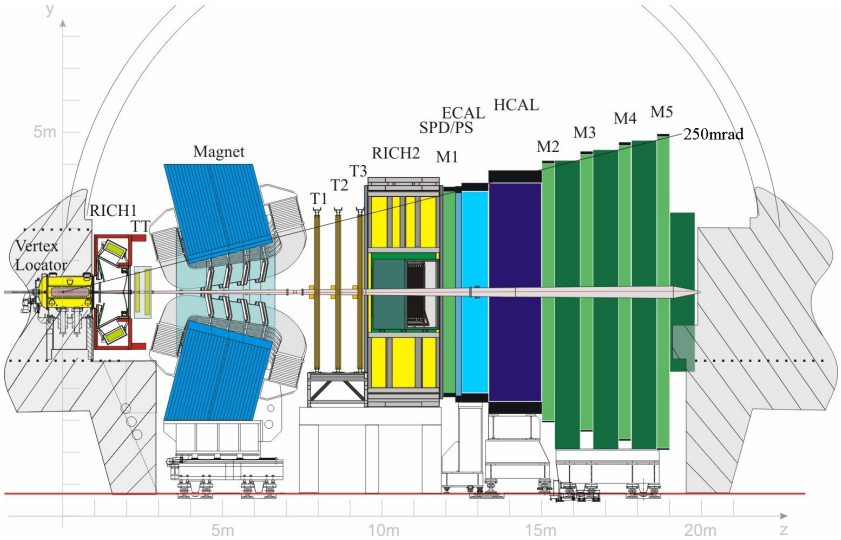

Figure 12: Schematic illustration of the side view of the LHCb-detector: The proton-proton collision takes place on the left in the Vertex Locator(VELO); RICH1 and RICH2 are Cherenkov detectors; TT is the Trigger Tracker, T1 - T3 the main tracking system, SPD is the Scintillating Pad Detector and PS the Preshower detector; ECAL is the electromagnetic calorimeter, HCAL the hadronic calorimeter and M1 - M5 the muon chambers

In the right-handed coordinate system, the z-axis is equal to the beam axis and the y-axis is along the vertical of the cavern.

- The proton-proton collision takes place on the left within the Vertex Locator(VELO), a silicon strip detector with excellent vertex resolution to resolve the proton-proton interaction point. A characteristic feature of the B- and D-mesons is their relatively long lifetime in the order of 1 ps, so that they fly a significant distance before decaying at the displaced secondary decay vertices which makes it easier to select signal and supress background.

- The Ring Imaging Cherenkov counters (RICH1 and RICH2) are used to identify particles via Cherenkov radiation.

- The magnet provides an integrated field of 4 Tm to bend the charged particles in order to determine their momenta. There is almost no material within the magnet at which the particles would scatter.

- The tracking system of the LHCb-detector is essential to reconstruct a decay signature, measure momenta and determine the decay time of a particle. It consists of a Trigger Tracker (a silicon microstrip detector, TT) in front of the magnet and three main tracking stations behind (T1 - T3). Their inner part with the highest detection rate, the Inner Tracker (IT), is made of silicon microstrips and the outer part, the Outer Tracker(OT) consists of a straw tube gas detector.

- The calorimeter system is used to measure the energy deposited by electromagnetic and hadronic showers but is more important to deliver trigger signals. It consists of a Scintillator Pad and a Preshower(SPD/PS) detector and an electromagnetic (shashlik type) calorimeter (ECAL) followed by a hadronic (Fe and scintillator tiles) calorimeter (HCAL).

- The muon detection system (M1 -M5) is composed of multi-wire proportional chambers (MWPC) and triple gas electron multipliers (GEM) in the region with the highest detection rate.

2.0.1 Vertex Loacator(VELO)

Immediately close to the proton-proton interaction point, the first detector is a silicon strip detector called the Vertex Locator(VELO). It consists of 25 disk-shaped silicon modules, each measuring the radial r and azimuthal ϕ coordinates of the particle tracks. A sketch of one VELO disk is given in Fig. 13 (left) and their arrangement on the right that are taken from [6].

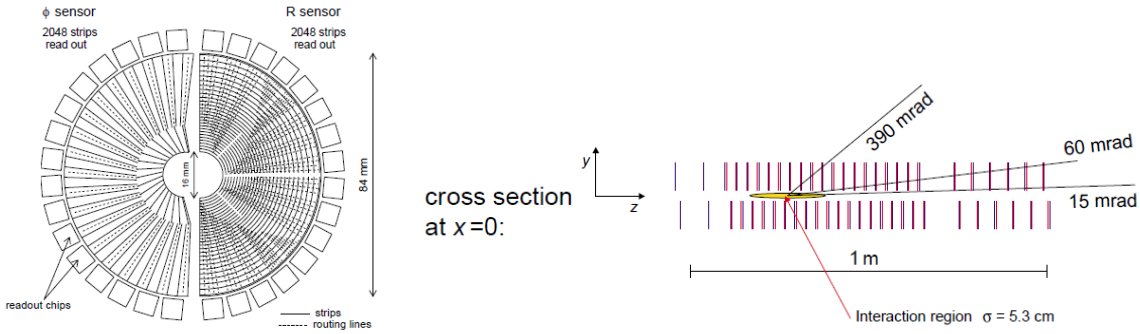

Figure 13: Sketch of the Vertex Locator(VELO) disk

During the nominal run, the two VELO halves are moved together and approach the nominal beam axis up to a distance of 5 mm [6] with the sensitive area starting at a radius of 8 mm. During the injection of the proton bunches into the LHC, the VELO halves can be moved 6 cm apart from the center to protect them from the beam. The excellent

vertex resolution is used to resolve the proton-proton interaction point, the primary vertex and the displaced secondary decay vertices that are a characteristic feature of B- and D-mesons.

2.0.2 Particle Identification

At LHCb, it is essential to distinguish pions and kaons that are produced numerously in the decays of B- and D-mesons. The two Ring Imaging Cherenkov counters in front of and behind the magnet (RICH1 and RICH2) detect the Cherenkov radiation that is emitted when charged particles traverse a dense medium with the refractive index n. This happens when the velocity $v = \beta c$ is larger than the light velocity $c' = \frac{c}{n}$ in the medium. The Cherenkov radiation is emitted in a cone of an angle θ around the flight direction of the particle:

$$\cos\theta = \frac{c'}{v} = \frac{1}{n\beta}.$$

The velocity βc can be determined by measuring the angle θ. By comparing the measured momentum and the velocity of the particle, the particle's mass and furthermore the particle type can be determined as it is shown in Fig. 14.

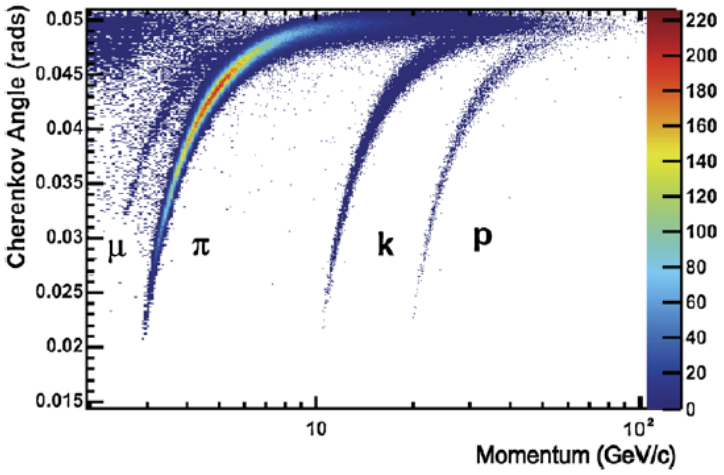

Figure 14: Cherenkov angle as a function of momemtum for different particle species taken from [7]

The information provided by the two RICH detectors, the calorimeters and the muon chambers is combined to a particle hypothesis in the form of a likelihood $\mathcal{L}(\pi,\ \mu\ or\ K)$. Since pions are produced most frequently in the proton-proton collisions, the difference of the logarithmic likelihood for a particle X and a pion are computed as the relative particle hypothesis

$$\Delta ln\mathcal{L}_{X-\pi} = ln\mathcal{L}(X) - ln\mathcal{L}(\pi). \tag{22}$$

This variable can be used to separate particles X from pions and is also called PID_X. An example is given by two-body hadronic decays $B^0 \to h^+h^-$, where h indicates a charged hadron. Without the RICH particle information, the events are composed of multiple contributions from kaons, pions and protons as shown in the invariant di-pion mass distribution on the left of Fig. 15. Applying a PID cut to select pions on the right, the background modes can be suppressed and the components separated.

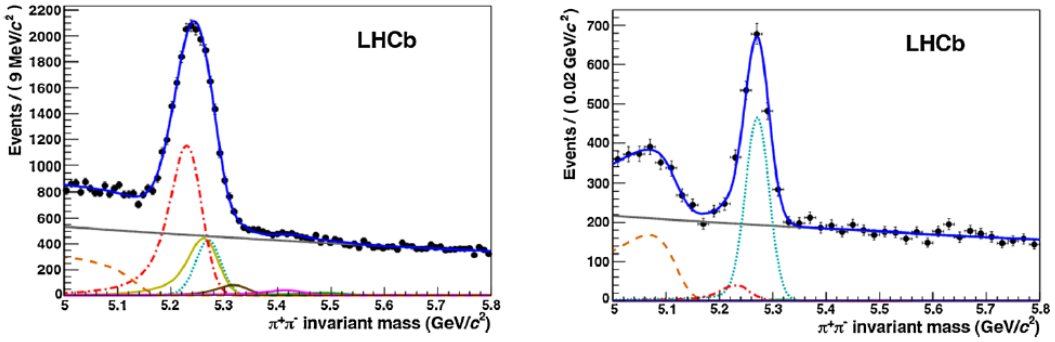

Figure 15: Invariant di-pion distribution without RICH(left) and with RICH(right) information: *dotted*: $B^0 \to \pi^+\pi^-$ signal; *dashed – dotted*: $B^0 \to K^+\pi^-$, dashed: 3-body; *line*: $B_s \to K^+K^-$, *line*: $B_s \to K^+\pi^-$; *line*: $\Lambda_b \to pK^-$; *line*: $\Lambda_b \to p\pi^-$ taken from [7]

2.0.3 Event reconstruction

The information provided by the detector components is used to reconstruct the event and the relevant decays like $B_s^0 \to \phi\phi$. The 4-momentum vector P of a particle consists of the energy $E = \sqrt{m^2 + \vec{p}^2}$ and the 3-momentum vector $\vec{p}$. Since the masses m of the decay products are not directly measured, the corresponding values of the PDG are assigned as the particle masses according to the particle hypothesis. Thus, the resulting 4-momentum is computed as[1]

$$\begin{aligned} P &= (E,\ \vec{p}) \\ &= \left(\sqrt{m_{PDG}^2 + \vec{p}^2},\ \vec{p}\right). \end{aligned} \tag{23}$$

A large fraction of the pions, kaons and muons are produced directly at the proton-proton interaction point. This vertex is reconstructed as the primary vertex (PV).
To reconstruct the decay $B_s^0 \to \phi\phi$, the tracks of the decay products, the two kaons are used to reconstruct the decay vertex of one ϕ.[2] The quality of the vertex reconstruction fit is described by the reduced vertex fit χ^2, i.e. the $\chi^2/nDof$. This quantity is called the

[1] in natural units
[2] The 4-momentum vector ϕ is calculated as the sum of the muon 4-momenta $P_\phi = P_{K^+} + P_{K^-}$.

vertex $\chi^2/nDof$.
Since the ϕ meson decays via the strong interaction, the lifetime is so short that it seems to decay immediately. Thus, the combined vertices are used to reconstruct the decay vertex (DV) of the B_s^0 meson as it is sketched in Fig. 16.[3] Due to the long B_s^0 lifetime of ≈ 1.5 ps it decays significantly away from the primary vertex.

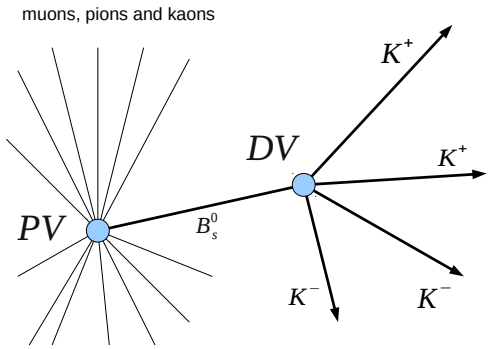

Figure 16: Illustration of the reconstruction of the decay $B_s^0 \to \phi\phi$

Denoting $\vec{d}_{pr}$ as the determined primary vertex, $\vec{d}_{decay}$ as the decay vertex and $d = \left|\vec{d}_{decay} - \vec{d}_{pr}\right|$ as the B_s^0 flight distance with the velocity[4] β, and $\gamma = 1/\sqrt{1-\beta^2}$ as in special relativity theory, the decay time t_{dec} of the B_s^0 can be computed as

$$\begin{aligned}
& t_{dec} = \frac{d}{\gamma v} \\
\Leftrightarrow \quad & t_{dec} = d\sqrt{\frac{1}{\beta^2} - 1} = \; d\sqrt{\left(\frac{E}{p}\right)^2 - 1} \\
\Leftrightarrow \quad & t_{dec} = \frac{d}{p}\sqrt{E^2 - p^2} = \; \frac{md}{p} \; = \; \frac{m\vec{d}\cdot\vec{p}}{|\vec{p}|^2} \\
\Leftrightarrow \quad & t_{dec} = \frac{m(\vec{d}_{decay} - \vec{d}_{pr})\cdot\vec{p}}{|\vec{p}|^2}
\end{aligned} \tag{24}$$

2.1 Triggers

Due to the high event rate of 40 MHz, events saved and used at LHCb are required to pass trigger requirements in three stages until the rate of storage is reduced to 5 kHz. The first one, level-0(L0), is provided by a hardware trigger that searches for high-E_T/p_T

[3]The B_s^0 4-momentum is the sum of the two ϕ 4-momenta $P_{B_s^0} = P_\phi + P_\phi$.
[4]in natural units

signatures using the calorimeters and the muon system. Charged tracks can be roughly divided into muons, electrons, photons and hadrons. The following two stages(Hlt1/2) are offline software triggers on computer farms that scan the recorded data using the tracking and particle identification information to reconstruct vertices.

3 Dataset

The following plots, tables and figures are taken from last year's paper [8].

3.1 Data selection

For this analysis, the data set consists of the full LHC run I of $1.1 fb^{-1}$ of 2011 and $2.0 fb^{-1}$ of 2012 collected events. The hadron trigger is used to find recorded hadron tracks but it does not distinguish between kaons and pions. At Hlt2-level, the tracks are used to reconstruct vertices that can originate from a ϕ meson (Hlt2IncPhi trigger) or exhibit at least three tracks (topological three-body trigger). Due to the small efficiency of the individual triggers, not all of these are required simultaneously, but they can be issued independently. In total, there are four disjoint ways an event can be triggered on signal (TOS):

- LOHadronTOS && Hlt2IncPhiTOS
- !LOHadronTOS && Hlt2IncPhiTOS
- LOHadronTOS && !Hlt2IncPhiTOS
- !LOHadronTOS && !Hlt2IncPhiTOS,

where an event without Hlt2IncPhiTOS trigger decision has to be issued by the three-body topological trigger. To isolate the signal sample from these events, simulated signal events are used to tune major kinematic selection cuts that are given in Table 1. Light particles like kaons tend to exhibit a larger transverse momentum p_T when they originate from the decay of a heavier B meson whereas particles from the primary vertex mostly keep their longitudinal momentum from the beam energy. The impact parameter(IP) is the distance of the prolongation of a track to the primary vertex and the $\mathrm{IP}_{sig} = IP/\sigma_{IP}$ refers to the significance. It is small for particles originating from the primary vertex whereas the long-lived B_s^0 meson mostly decays a significant distance away from the primary vertex. The invariant di-kaon mass is required to be close to the known ϕ mass and the vertices have to be reconstructed with an appropriate fit value. At last, it is essential to apply a PID_K selection because the hadron trigger includes pion tracks.

However, this is only a rough selection and the events are still heavily polluted by background, mainly from combinatorics but also from other decays where one of the kaons might have been mis-identified. To further isolate the signal, a separate multi-variate analysis technique, precisely a boosted decision tree (BDT), with event-dependent selection

variable	selection cut
Track p_T	> 400 MeV/c
Track IP^2_{sig}	> 25
PID_K	> -5
$\lvert M_{KK} - M_{\phi}^{PDG} \rvert$	< 25 MeV/c^2
ϕ^1 p_T $\times$ ϕ^2 p_T	$> 2\,\mathrm{GeV}^2/c^2$
ϕ vertex χ^2 per NDF	< 15
B_s^0 vertex χ^2 per NDF	< 15

Table 1: Summary of the major selection cuts for the $B_s^0 \to \phi\phi$ decay.

cuts is used that is trained on a simulated and fully reconstructed signal sample. The background sample is obtained from data where the four-kaon invariant mass does not lie within a mass window of 120 MeV/c^2 around the known B_s^0 mass of ≈ 5360 MeV/c^2. Using several kinematic distributions, this classifier compares typical event signatures and effectively selects the signal while discriminating against background. The output is a dimensionless response.

The variables with the largest separation power are:

- B_s^0 vertex χ^2 per NDF
- kaon and ϕ transverse momentum
- PID_K
- cosine of the angle between the direction of the momentum and the flight direction of the B_s^0

The invariant mass distribution of the selected four-kaon events is shown in Fig. 17, separately for the 2011 and the 2012 datasets, and exhibits a clean signal peak at the known B_s^0 mass with only small background. The fit function is a sum of two Gaussian functions and linear background

3.2 Peaking background components

However, two contributing resonant background components are still among these selected events. The first one is the decay $B^0 \to \phi K^*(\to K\pi)$, where one pion is mis-identified as a kaon. The other contribution comes from $\Lambda_b^0 \to \phi K p$ events where the proton is mis-identified as a kaon. To investigate their contributions, the mass hypothesis of the involving particles is changed, e.g. the kaon mass of one particle is replaced by the proton mass. The signal peak in this resultant mass distributions gives the number of background events.

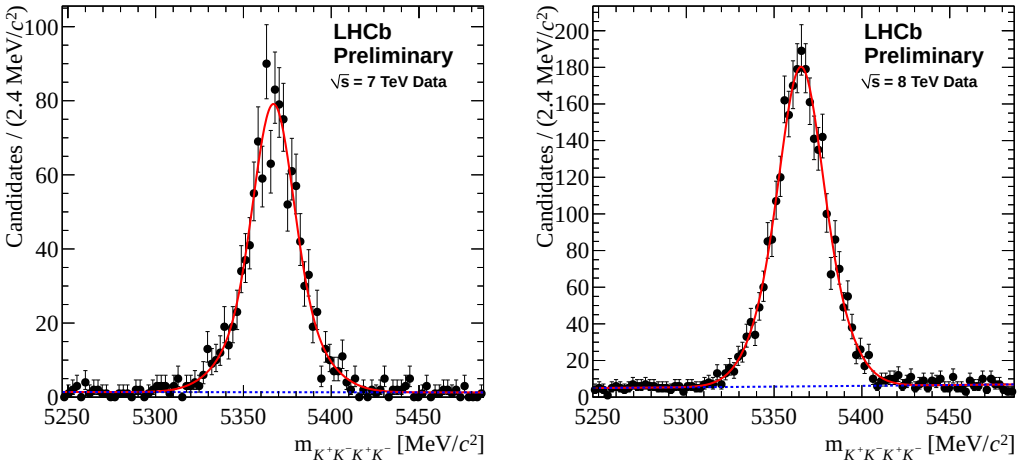

Figure 17: Four-kaon invariant mass distributions for the fully selected 2011 (left) and 2012 (right) datasets described by the sum of two Gaussian functions and linear background.

3.2.1 Contribution from $\Lambda_b^0 \to \phi K p$

To estimate the total Λ_b contribution, these selected events are reconstructed under the hypothesis that one of the four final particles is a proton. Doing this, the invariant mass distribution changes and gets distorted and shifted to larger values. The effect on the signal $B_s^0 \to \phi\phi$ shape is determined using a fully simulated signal sample reconstructed under the same particle hypothesis in in Fig. 18. It has an asymmetric peak and a long tail towards higher invariant masses.

The selected data is shown in Fig. 19, separated in the two years where a small peak around the known Λ_b mass can be identified on top of the $\phi\phi$ shape. A fit using the simulated signal shape and a single Gaussian function yields contributions of 52 ± 19 and 51 ± 29 $\Lambda_b^0 \to \phi K p$ events among the selected data.

When applying harder cuts on the proton identification to suppress the signal decay, a clear Λ_b peak in the mass distribution can be seen in Fig. 20.

3.2.2 Contribution from $B^0 \to \phi K^*(\to K\pi)$

The $B^0 \to \phi K^*$ component among the selected events is smaller than the Λ_b contribution and cannot be determined with the above-described procedure. Therefore, the number of events is estimated using simulated $B^0 \to \phi K^*$ decays and a new data selection designed to find the ϕK^* signal by applying inverted PIDK cuts for the pion. It is assumed that the following ratios are equal for data and simulation reconstructed under the $\phi K\pi$ hypothesis:

$$\frac{\#\text{ of } \phi K^* \text{ in } \phi\phi \text{ data selection}}{\#\text{ of } \phi K^* \text{ in } \phi K^* \text{ data selection}} = \frac{\#\text{ of } \phi K^* \text{ in } \phi\phi \text{ selection in } \phi K^* \text{ MC}}{\#\text{ of } \phi K^* \text{ in } \phi K^* \text{ selection in } \phi K^* \text{ MC}}, \tag{25}$$

where the number of ϕK^* in $\phi\phi$ data selection is too small to be determined in the

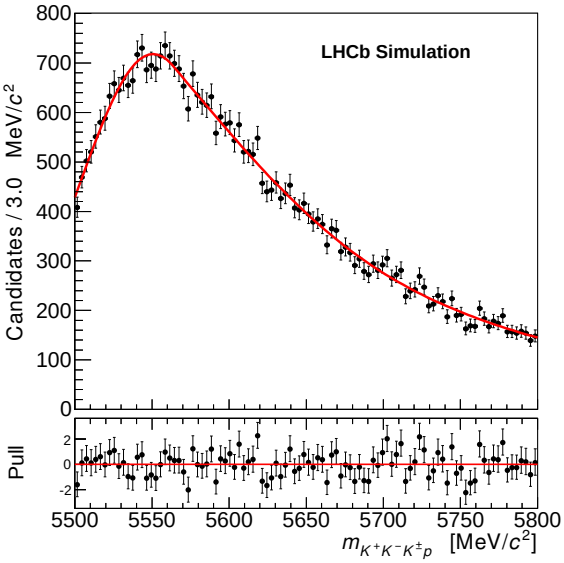

Figure 18: $B_s^0 \to \phi\phi$ simulation reconstructed as $\Lambda_b^0 \to \phi K p$.

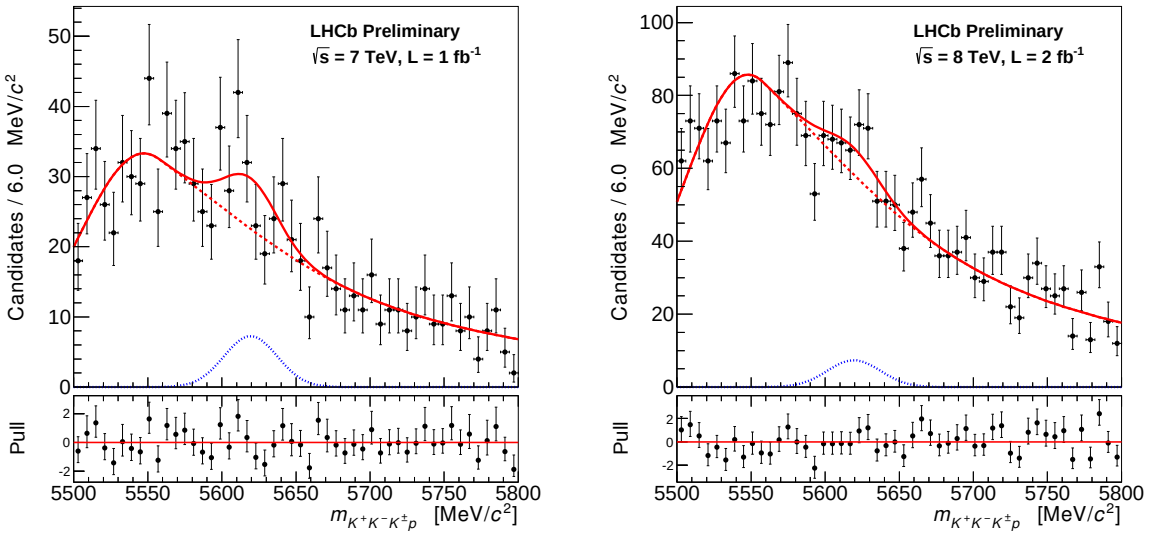

Figure 19: 2011 (left) and 2012 (right) data reconstructed as $\Lambda_b^0 \to \phi K p$. The total PDF, $B_s^0 \to \phi\phi$ component, and $\Lambda_b \to \phi K^- p$ component are given by the red solid, red dotted, and blue dotted lines, respectively.

distribution and the other numbers can be measured. Inserting the determined quantities yields 2011 and 2012 numbers of ϕK^*events among the $\phi\phi$ data selection of 7.3 ± 0.4 and 17.8 ± 0.9, respectively.

Using the extracted yields and shapes of the peaking backgrounds, the fit to the selected

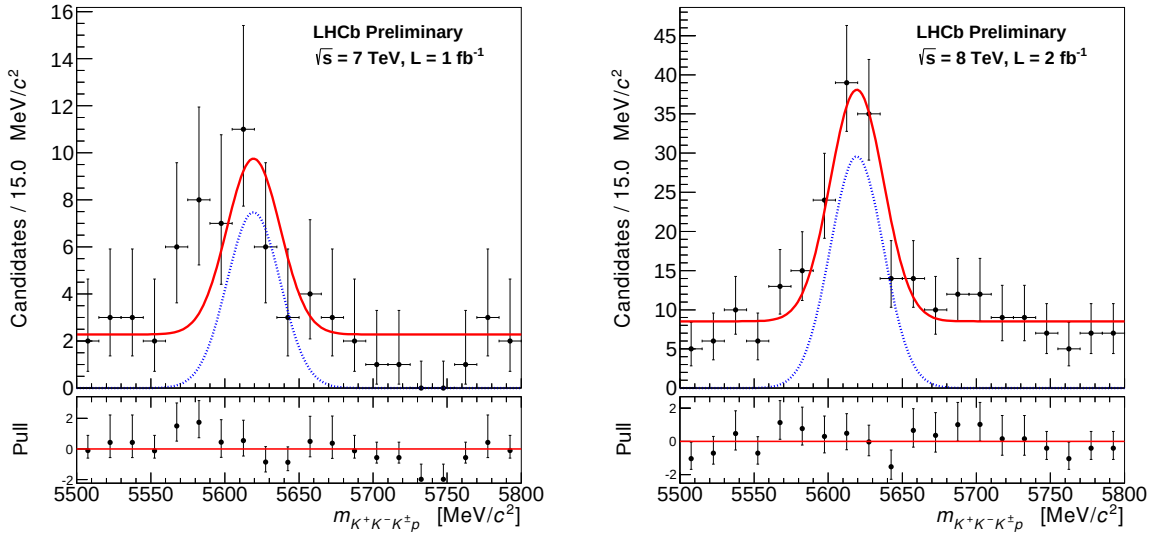

Figure 20: Fits to the 2011 (left) and 2012 (right) data under the ϕKp hypothesis with a harder cut on DLL_p applied to the proton candidate in each event. The total PDF and $\Lambda_b \to \phi K^- p$ component are given by the red solid and blue dotted lines, respectively.

$\phi\phi$ data is shown in Fig. 21.

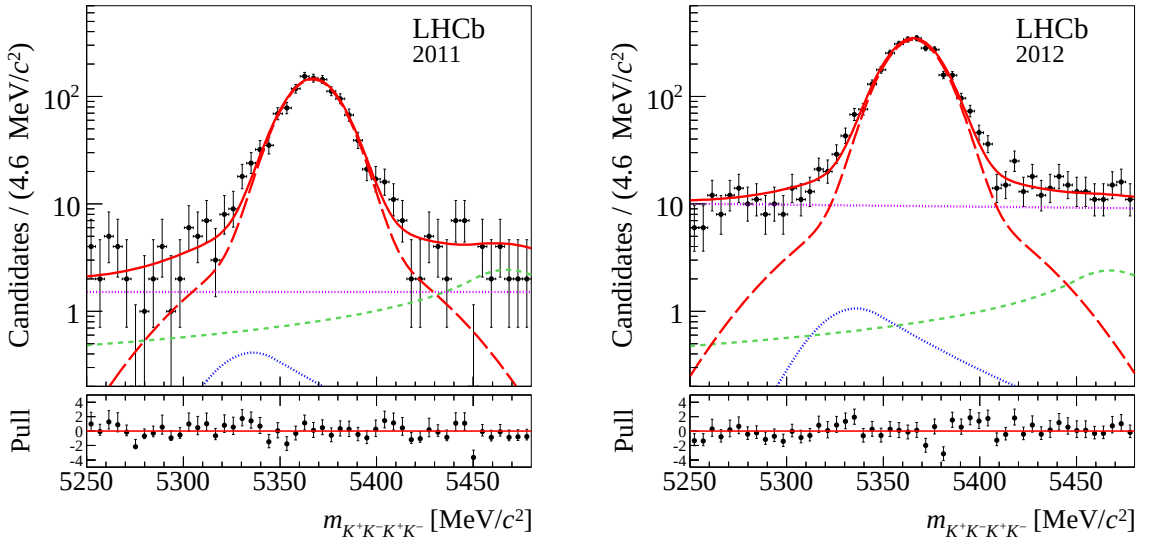

Figure 21: A fit to the 2011 (left) and 2012 (right) $\phi\phi$ data including the $B^0 \to \phi K^*$ and $\Lambda_b^0 \to \phi Kp$ reflections. The data is represented by the black points. Superimposed are the results of the total fit (red solid line), the $B_s^0 \to \phi\phi$ (red long dashed), the $B^0 \to \phi K^{*0}$ (blue dotted), the $\Lambda_b \to \phi p K^-$ (green short-dashed), and the combinatoric (purple dotted) fit components.

This fit is used to assign weights to every event according to its invariant four-kaon mass such that all the background, combinatorial and peaking, is statistically subtracted from the sample. These weights are called sweights. From now on, this so-called sweighted selected data sample consists of a pure $B_s^0 \to \phi\phi$ signal sample without combinatorial and peaking background contributions.

3.3 Excursion on sweights

To illustrate the use of sweights, a small example taken from [9] is discussed here. Assume the mass of your selected events is distributed as shown in the upper left plot in Fig. 22.

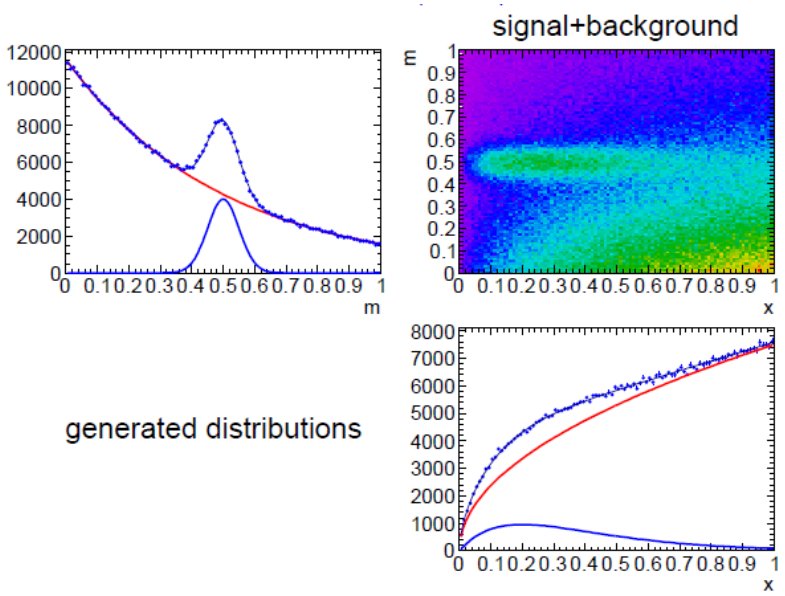

Figure 22: Generated mass distribution (top left) with a Gaussian peak, exponential background and corresponding x distribution (bottom right) and the two-dimensional distribution(top right)

There is a clear signal peak at 0.5 a.u. in blue superimposed with some exponential, perhaps combinatorial, background in red. The x distribution of these events with the two components is given in the lower right. One can imagine that if you subtract the background distribution from the overall distribution, this results in the signal distribution. For this reason, you can define two mass regions in Fig. 23 with equal widths for which you assign a positive(signal) and a negative(background) weight. Then, the x distribution of the sidebands region is subtracted from the x distribution in the signal region. Of course this is only an approximation and assumes a linear increase of the background towards lower mass.

A more correct way is to assign a weight, called sweight w(m), to every event as given on the right in Fig. 24 according to the above mass fit. Events with an invariant mass around the peak region have a positive weight whereas distant events have negative weights.

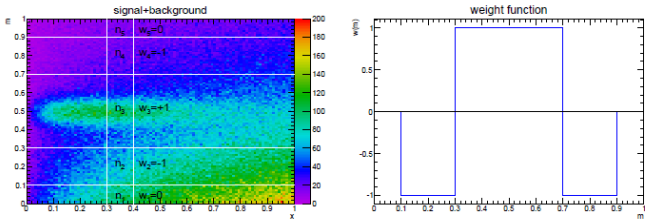

Figure 23: Two-dimensional m-x distribution of generated events divided into a signal(weight +1) and a background(weight -1) mass region

Applying these weights to the x distribution results in background-subtracted pure signal distribution on the left.

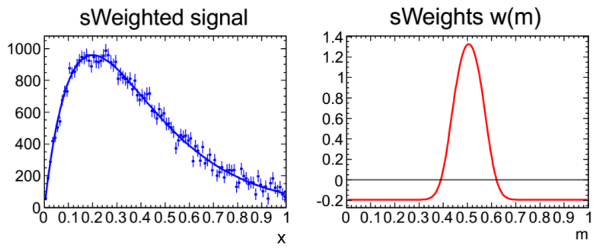

Figure 24: Assigning weights(right) according to mass fit of Fig. 22 and applying these on the x distribution(left)

4 Determination of time acceptance correction

As discussed before, the event selection profits from the fact that the B_s^0 lifetime is so large that the flight distance from the production to the decay vertex can usually be resolved. Decays in which the the kaons appear to originate from the primary vertex, are removed to suppress prompt background. However, these selection cuts also reject signal events with very small decay times so that the decay time distribution becomes distorted. The *decay time acceptance* describes the efficiency of selecting the signal decays as a function of decay time t and can be defined as the decay time-dependent ratio of selected and produced signal particles:

$$\epsilon_{time}(t) = \frac{\#\ of\ selected\ B_s^0\ (t)}{\#\ of\ produced\ B_s^0\ (t)}. \tag{26}$$

In data, the total number of produced B_s^0 is not known but it could be accessed in simulation. Though, instead of purely relying on simulation, it is preferred to use data-driven methods to determine the corrections. Therefore, the topologically similar

channel $B_s^0 \to D_s^+(\to \phi\pi^+)\ \pi^-$, where two kaons are simply replaced by two pions in the final state, is used as a control mode to model the time acceptance. The advantages of this decay are the excellent signal-to-background ratio and the higher statistics, but the number of produced B_s^0's is not known as well. Thus, the acceptance $\epsilon_{time}(t)$ has to be determined by comparing the measured simulated decay time distribution $d\Gamma_{mes}/dt$ with the theoretical prediction $d\Gamma_{theo}/dt$. The acceptance is proportional to the ratio $d\Gamma_{mes}/d\Gamma_{theo}$

$$\epsilon_{time}(t) \ \propto \ \frac{d\Gamma_{mes}(t)}{d\Gamma_{theo}(t)}. \tag{27}$$

In order to match the decay topology, the event selection and the multi-variate analysis to isolate the $B_s^0 \to D_s^+\ \pi^-$ signal use the same cuts as for $B_s^0 \to \phi\phi$ decays except for the particle identification requirements for the pions.[2]

Due to the small efficiency of one single trigger, the data sample profits from several triggers that can be issued independently. Yet, each trigger category requires different kinematic criteria that give rise to individual time acceptance corrections that have to be determined separately. Additionally, one has to prove that the channel $B_s^0 \to D_s^+\ \pi^-$ is subject to the same time acceptance as $B_s^0 \to \phi\phi$. The comparison of simulated $B_s^0 \to \phi\phi$ to $B_s^0 \to D_s^+\ \pi^-$ time acceptances is shown for the four trigger categories in Fig. 25. At small decay times, the efficiency steeply rises from zero and reaches a plateau at the maximum efficiency. The agreement between data and MC is fairly good and the small differences are accounted for as a systematic uncertainty.

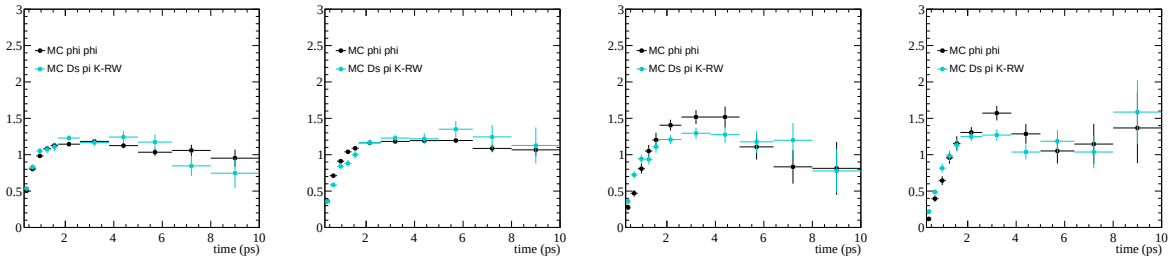

Figure 25: Comparison of simulated $B_s^0 \to \phi\phi$(black) events to simulated $B_s \to D_s\pi^+$(cyan) events for candidates triggered as (from left to right) HadronTOS and IncPhiTOS, !HadronTOS and IncPhiTOS, HadronTOS and !IncPhiTOS, !HadronTOS and !IncPhiTOS.

The time acceptance distributions determined from $B_s^0 \to D_s^+\ \pi^-$ 2012 data are given in Fig. 26. In the final fit for the CP-violating phase, these histograms are simply multiplied to the pdf.

[2]The decay is reconstructed as $B_s^0 \to D_s^+\ \pi^-$ and not as $B_s^0 \to \phi\phi$

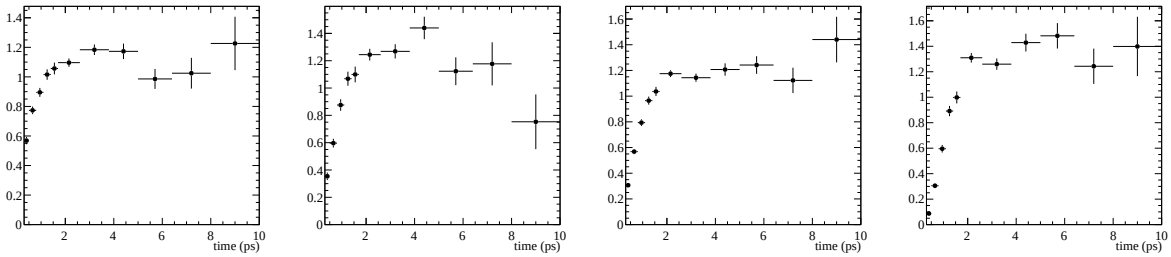

Figure 26: Decay time acceptance found from $B_s^0 \to D_s^+\pi^-$ 2012 data for candidates triggered as (from left to right) HadronTOS and IncPhiTOS, !HadronTOS and IncPhiTOS, HadronTOS and !IncPhiTOS, !HadronTOS and !IncPhiTOS.

5 Determination of the initial B_s^0 production flavour

Without the knowledge of the initial flavour state of the B_s^0-meson, it is impossible to resolve the B_s^0-$\bar{B}_s^0$ time oscillation in time and to perform a CP analysis. The determination of the initial B_s^0 production flavour is called *Flavour Tagging*. There are two different methods for tagging that are sketched in Fig. 27.

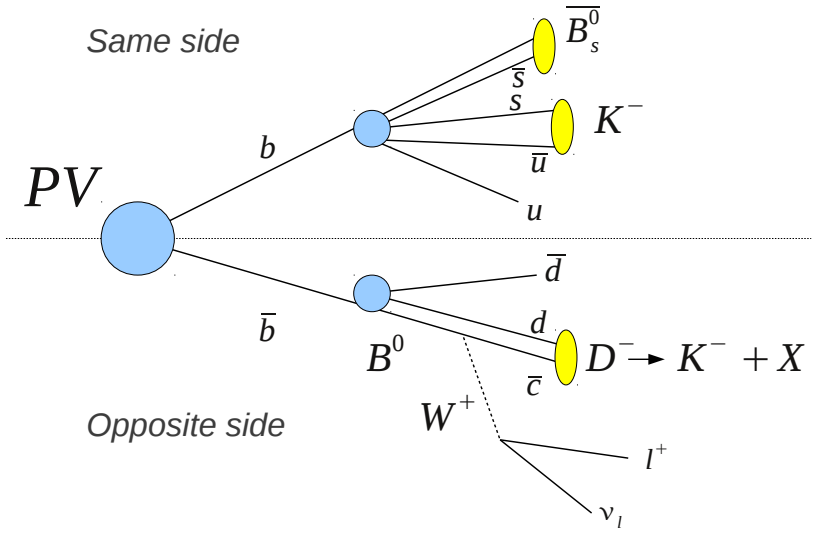

Figure 27: Illustration of the flavour tagging algorithms. In the upper part the same side tagger and below the opposite side tagger

- The *opposite* - *side* tagging algorithm sketched in the lower part of Fig. 27 profits from the fact that in proton-proton collisions, the b-quarks are produced as a quark−anti-quark pair. Whereas one of them hadronizes to become the signal $\bar{B}_s^0$, the other quark hadronizes to a B-hadron with opposite flavour that can decay

semileptonically into a D-meson, a lepton l and a neutrino ν_l. The flavour of the b-quark is then determined by the charge of the lepton l. Additionally, when the charmed meson decays into a kaon, the kaon charge can also be used to confirm the flavour. The combined tagging decision forms the *opposite-side tag*.

- The *same - side* tagging algorithm is sketched in the upper part. The s anti-quark that is used in the hadronization of the b-quark to form the signal $\bar{B}_s^0$, is produced together with an s-quark. The s-quark hadronizes and can form a K-meson close to the signal $\bar{B}_s^0$. The charge of the kaon can be used to determine the flavour of the initial b-quark. This algorithm is called the *same-side kaon tagger* or shortly the same-side tagger. If the signal B-meson is a B^0, the same side tagger uses pions that are created in the vicinity.

The flavour tag decision q provided by the taggers is defined as q = 1 for a tagged B_s^0, q = -1 for a $\bar{B}_s^0$ and q = 0 for an unsuccessful tag. Since the algorithms are not perfect, the mistag probability ω_{tag} gives the probability that the algorithm has assigned the wrong tag decision where an ω_{tag} of 0.5 already means that the decision is completely random. Thereby, the possibility of the other B meson to oscillate is the largest source of wrong assignment. The dilution that dilutes the B_s^0-$\bar{B}_s^0$ oscillation is defined as $D_{tag} = (1 - 2\,\omega_{tag})$. For every event, the mistag probability is estimated by the tagging algorithms based on the occurring kinematics and is denoted as ω_{est}. Furthermore, the taggers are not always able to provide a tag decision. The tagging efficiency ϵ_{tag} therefore indicates the ratio of events for which the tagging algorithms are able to deliver a tagging decision:

$$\epsilon_{tag} = \frac{number\ of\ tagged\ events}{number\ of\ all\ events} = \frac{N_{tagged}}{N}. \tag{28}$$

The effective tagging power $\mathcal{P}_{tag}^{eff} = \epsilon_{tag}\ D_{tag}^2$ is the measure for the statistical power of the events if tagging is considered. Considering a per-event determination of the mistag probabilities, it is computed as

$$\mathcal{P}_{tag}^{eff} \;=\; \epsilon_{tag}\left\langle D_{tag}^2 \right\rangle \;=\; \frac{N_{tagged}}{N}\,\frac{1}{N_{tagged}}\sum_{i=1}^{N_{tagged}}(1-2\omega_{i,est})^2 = \;\frac{1}{N}\sum_{i=1}^{N_{tagged}}(1-2\omega_{i,est})^2. \tag{29}$$

Note that the typical effective tagging power at LHCb is only about 3-5%. The B-factories Belle and Babar were e^+e^- colliders where the centre-of-mass energy was tuned to the bottomonium resonances, mostly to Y(4S), which provides very clean events compared to the huge hadronic background as at the LHC. Thereby, the two b quarks from the coherent state are entangled until they decay and quantum numbers are conserved, i.e. they only mix simultaneously into the anti-quark. Thus, the typical tagging power at the B-factories of 40 % is much higher.

6 Determination of CP-value of the final state $\phi\phi$

The general decay rates for a B_s^0 and $\bar{B}_s^0$ meson into a final state f are given in Equations 19 and 20. Considering a final CP-eigenstate with CP-eigenvalue η_{CP} and defining the three CP-violating terms

$$C = \frac{1-\lambda^2}{1+\lambda^2}, \tag{30}$$

$$S = -\frac{2\lambda \sin\phi_s}{1+\lambda^2}, \tag{31}$$

$$D = -\frac{2\lambda \cos\phi_s}{1+\lambda^2}, \tag{32}$$

these equations can be transformed as

$$\begin{aligned}\frac{d\Gamma(B_s^0 \to f_{CP})}{dt N_f} &= |A_{CP}|^2\ e^{-\Gamma_s t}\ \frac{1}{1+C}\left\{\cosh\frac{\Delta\Gamma_s t}{2}\ +\ C\ \cos(\Delta m_s t)\right. \\ &\left. +D\eta_{CP}\ \sinh\frac{\Delta\Gamma_s t}{2} - S\eta_{CP}\ \sin(\Delta m_s t)\right\}\end{aligned} \tag{33}$$

and

$$\begin{aligned}\frac{d\Gamma(\bar{B}_s^0 \to f_{CP})}{dt N_f} &= |A_{CP}|^2\ e^{-\Gamma_s t}\ \frac{1}{1+C}\left\{\cosh\frac{\Delta\Gamma_s t}{2}\ -\ C\ \cos(\Delta m_s t)\right. \\ &\left. +D\eta_{CP}\ \sinh\frac{\Delta\Gamma_s t}{2} + S\eta_{CP}\ \sin(\Delta m_s t)\right\}.\end{aligned} \tag{34}$$

In the decay $B_s^0 \to \phi\phi$, the spin-0 B_s^0 decays into two spin-1 ϕ mesons, i.e. it is a pseudo-scalar to vector vector (P $\to$ V V) decay. For conserving the initial spin $\mathbf{J} = 0$, the final state mesons can have a relative angular momentum l of 0, 1 and 2. The final CP-eigenvalue η_{CP} is related to the angular momentum via

$$\eta_{CP} = (\eta_\phi)^2\ (-1)^l = (-1)^l. \tag{35}$$

Thus, the final state is not a CP-eigenstate but a mixture of CP-eigenstates that have to be separated in an angular analysis. Each angular momentum is related to an angular polarisation: 0: A_0, 1: $A_\perp$ and 2: $A_{||}$ as shown in Fig. 28.

The decay topology is described by the so-called helicity basis $(\theta_1, \theta_2, \Phi)$ shown in Fig. 29. The K^+ momentum in the $\phi_{1,2}$ rest frame, and the parent $\phi_{1,2}$ momentum in the rest frame of the B_s^0 meson span the two ϕ meson decay planes, $\theta_{1,2}$ is the angle between the K^+ track momentum in the $\phi_{1,2}$ meson rest frame and the parent $\phi_{1,2}$ momentum in the B_s^0 rest frame, Φ is the angle between the two ϕ meson decay planes and $\hat{n}_{1,2}$ is the unit vector normal to the decay plane of the $\phi_{1,2}$ meson. The angles θ correspond to the angle between the K^+ and the flight direction of the ϕ meson in the rest frame of the ϕ meson. In this analysis, the choice of which ϕ meson is used to determine θ_1 and which is used to determine θ_2 is randomised.

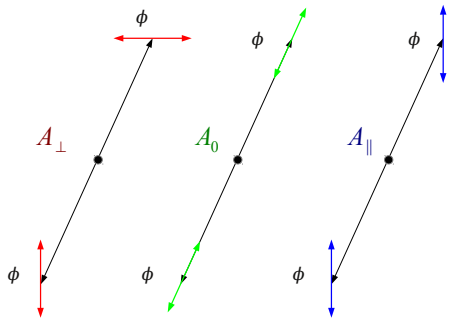

Figure 28: Illustration of the angular amplitudes referring to the relative angular momentum l of 0, 1, 2

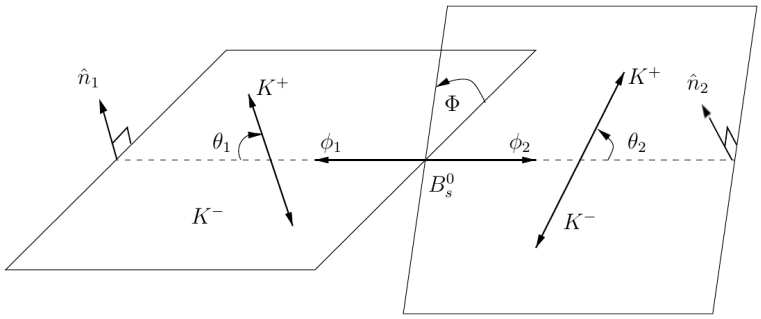

Figure 29: Decay topology of the decay $B_s^0 \to \phi\phi$ in the helicity basis

The total decay amplitude $A(t, \theta_1, \theta_2, \Phi)$ can be written as the sum of the angular decay rates as

$$A(t, \theta_1, \theta_2, \Phi) = A_0(t)\ \cos\theta_1 \cos\theta_2 + \frac{A_{||}(t)}{\sqrt{2}}\ \sin\theta_1 \sin\theta_2 \cos\Phi + i\ \frac{A_\perp(t)}{\sqrt{2}}\ \sin\theta_1 \sin\theta_2 \sin\Phi. \quad (36)$$

The total differential decay rate is computed as the absolute square of the decay amplitude

$$\frac{\mathrm{d}\Gamma}{\mathrm{d}t\ \mathrm{d}\cos\theta_1\ \mathrm{d}\cos\theta_2\ d\Phi} \propto |A(t, \theta_1, \theta_2, \Phi)|^2 = \sum_{i=1}^{6} \mathrm{K}_i(t)\ \mathrm{f}_i(\theta_1, \theta_2, \Phi), \quad (37)$$

where the functions $\mathrm{K}_i(t)$ are the exponential decay rates

$$K_i(t) = N_i e^{-\Gamma_s t}[c_i \cos(\Delta m_s t) + d_i \sin(\Delta m_s t) + a_i \cosh(\frac{1}{2}\Delta\Gamma_s t) + b_i \sinh(\frac{1}{2}\Delta\Gamma_s t)], \quad (38)$$

and the functions $\mathrm{f}_i(\theta_1, \theta_2, \Phi)$ are purely geometric angular functions. The 6 terms are composed of the 3 squared angular amplitudes and 3 interference terms. All the coefficients are given in Table 2, where the strong phase differences are defined to be $\delta_1 := \delta_\perp - \delta_{||}$ and $\delta_2 := \delta_\perp - \delta_0$.

i	N_i	a_i	b_i	c_i	d_i	f_i
1	$\|A_0\|^2$	1	D	C	$-S$	$4\cos^2\theta_1\cos^2\theta_2$
2	$\|A_\parallel\|^2$	1	D	C	$-S$	$\sin^2\theta_1\sin^2\theta_2(1+\cos 2\Phi)$
3	$\|A_\perp\|^2$	1	$-D$	C	S	$\sin^2\theta_1\sin^2\theta_2(1-\cos 2\Phi)$
4	$\|A_\parallel\|\|A_\perp\|$	$C\sin\delta_1$	$S\cos\delta_1$	$\sin\delta_1$	$D\cos\delta_1$	$-2\sin^2\theta_1\sin^2\theta_2\sin 2\Phi$
5	$\|A_\parallel\|\|A_0\|$	$\cos(\delta_{2,1})$	$D\cos(\delta_{2,1})$	$C\cos\delta_{2,1}$	$-S\cos(\delta_{2,1})$	$\sqrt{2}\sin 2\theta_1\sin 2\theta_2\cos\Phi$
6	$\|A_0\|\|A_\perp\|$	$C\sin\delta_2$	$S\cos\delta_2$	$\sin\delta_2$	$D\cos\delta_2$	$-\sqrt{2}\sin 2\theta_1\sin 2\theta_2\sin\Phi$

Table 2: Coefficients of the time-dependent terms and angular functions used in equation 37. Amplitudes are defined at $t = 0$.

In the first lecture, the decays $B_s^0 \to J/\Psi\phi$ and $B_s^0 \to J/\Psi f_{0/2}$ were given as examples to measure CP-violation in the interference of the decay and the decay after mixing. Wheres the first one is also a P $\to$ V V decay, the spin of the f-resonance is even which requires the relative angular momentum l to be 1 or 3. Thus, the final state is an odd CP-eigenstate, the angular analysis is not necessary and the statistical sensitivity to ϕ_s is higher. Although the $J/\Psi f_{0/2}$ statistics(35000) is only 1/3 of $J/\Psi\phi$(100000), the statistical uncertainties on the ϕ_s measurement are comparable (0.068 and 0.049 rad). Assuming the statistical uncertainty decreases with $\sqrt{N}$, the sensitivity to ϕ_s is about 20 % better without angular analysis.

6.1 Contribution from K^+K^- in an S-wave state

Experimentally, a pure $B_s^0 \to \phi\phi$ signal sample cannot be selected because other resonances like the $f_0(980)$ within the ϕ mass range that decay into the same final state, K^+K^-, or non-resonant kaons contribute to the selected events. For this reason, the K^+K^- system can also be found in an S-wave, i.e. spin-0, resonant or non-resonant state that cannot be discriminated against. Therefore, this S-wave contribution has to be included in the angular analysis. Besides the additional PS-wave component $B_s^0 \to \phi(K^+K^-)_S$, the two kaon pairs can also be simultaneously found in an S-wave state leading to an SS-wave component $B_s^0 \to (K^+K^-)_S(K^+K^-)_S$. The additional S-wave amplitudes are given by

$$A_{S/SS}(t,\theta_1,\theta_2,\Phi) = \frac{A_S(t)}{\sqrt{3}}\ (\cos\theta_1 + \cos\theta_2) + \frac{A_{SS}(t)}{3}. \tag{39}$$

After adding these terms to the signal P-wave contribution, the absolute square exhibits 15 terms:

$$\frac{\mathrm{d}\Gamma}{\mathrm{d}t\mathrm{d}\cos\theta_1\mathrm{d}\cos\theta_2 d\Phi} \propto |A(t,\theta_1,\theta_2,\Phi)|^2 = \sum_{i=1}^{15} \mathrm{K}_i(t)\ \mathrm{f}_i(\theta_1,\theta_2,\Phi), \tag{40}$$

the 6 P-wave terms in Table 2, the S and SS-wave terms with interferences in lines 7-9 of Table 3, the SS-P-wave interference terms in lines 10-12 and the S-P-wave interference

terms in lines 13-15.

7 Determination of angular acceptance correction

For the separation of the CP-eigenstates, the determination of the angular distributions in the helicity basis is crucial. However, the detector is not a homogeneous object but built from different sub-components with well defined sensitive areas. The *angular acceptance* ϵ_{acc} describes the efficiency of the particle detection as a function of the helicity angles and is defined as the ratio of the number of reconstructed and accepted events N_{acc} to the total number of events N_{event}:

$$\epsilon_{acc}(\cos\theta_1, \cos\theta_2, \Phi) \;=\; \frac{N_{acc}(\cos\theta_1, \cos\theta_2, \Phi)}{N_{event}(\cos\theta_1, \cos\theta_2, \Phi)}. \tag{41}$$

The detector acceptance has been intensively studied and is taken into account in the detector simulations. Hence, the number of accepted events as a function of the angles can be determined in simulated $B_s^0 \to \phi\phi$ decays. However, the acceptance effects are already accounted for in the generation of the simulated events to reduce the computational effort. The total number of events as a function of the angle cannot be computed. Thus, the acceptance ϵ_{acc} has to be determined by comparing the measured simulated angular distribution $d\Gamma_{mes}/dt$ with the theoretical prediction $d\Gamma_{theo}/dt$. The acceptance is proportional to the ratio $d\Gamma_{mes}/d\Gamma_{theo}$

$$\epsilon_{acc}(\cos\theta_1, \cos\theta_2, \Phi) \;\propto\; \frac{d\Gamma_{mes}(\cos\theta_1, \cos\theta_2, \Phi)}{d\Gamma_{theo}(\cos\theta_1, \cos\theta_2, \Phi)}. \tag{42}$$

Note that this is not the absolute detection efficiency but the relative efficiency and only the shape is of importance. The 1-dimensional projections of the angular acceptance correction for each angle are drawn in Fig. 30. Whereas it is flat in Φ, there is a clear drop in efficiency towards $\cos\theta_i \to \pm\,1$ which is mainly caused by the selection cuts of the transverse momenta on the kaons. Technically, the shape is used to correct the angular functions f_i in Table 3.

8 Coupling of S- and P- wave

When talking about the interference of P-wave and S-wave terms, a few details were detained for simplicity, precisely the mass dependence of the individual amplitudes $A_i(m_{KK})$. Clearly, when two components are far apart in the invariant mass, the interference must be small as a consequence. This can be accounted for by an effective coupling factor C_{SP} that is multiplied to the interference terms in the decay rate but this is just an average. One solution is to divide the data sample into many bins of the invariant KK spectrum for which the mass-dependence is constant. The effective coupling correction $C_{SP} \to 1$ but for each bin an individual S-wave amplitudes has to be fitted. However, spreading the statistics over many bins does not allow fitting numerous amplitudes. For this reason,

i	N_i	a_i	b_i	c_i	d_i	f_i
7	$\lvert A_{SS}\rvert^2$	1	D	C	$-S$	$\frac{4}{9}$
8	$\lvert A_S\rvert^2$	1	$-D$	C	S	$\frac{4}{3}(\cos\theta_1+\cos\theta_2)^2$
9	$\lvert A_S\rvert\lvert A_{SS}\rvert$	$C\cos(\delta_S-\delta_{SS})$	$S\sin(\delta_S-\delta_{SS})$	$\cos(\delta_{SS}-\delta_S)$	$D\sin(\delta_{SS}-\delta_S)$	$\frac{8}{3\sqrt{3}}(\cos\theta_1+\cos\theta_2)$
10	$\lvert A_0\rvert\lvert A_{SS}\rvert$	$\cos\delta_{SS}$	$D\cos\delta_{SS}$	$C\cos\delta_{SS}$	$-S\cos\delta_{SS}$	$\frac{8}{3}\cos\theta_1\cos\theta_2$
11	$\lvert A_\parallel\rvert\lvert A_{SS}\rvert$	$\cos(\delta_{2,1}-\delta_{SS})$	$D\cos(\delta_{2,1}-\delta_{SS})$	$C\cos(\delta_{2,1}-\delta_{SS})$	$-S\cos(\delta_{2,1}-\delta_{SS})$	$\frac{4\sqrt{2}}{3}\sin\theta_1\sin\theta_2\cos\Phi$
12	$\lvert A_\perp\rvert\lvert A_{SS}\rvert$	$C\sin(\delta_2-\delta_{SS})$	$S\cos(\delta_2-\delta_{SS})$	$\sin(\delta_2-\delta_{SS})$	$D\cos(\delta_2-\delta_{SS})$	$-\frac{4\sqrt{2}}{3}\sin\theta_1\sin\theta_2\sin\Phi$
13	$\lvert A_0\rvert\lvert A_S\rvert$	$C\cos\delta_S$	$-S\sin\delta_S$	$\cos\delta_S$	$-D\sin\delta_S$	$\frac{8}{\sqrt{3}}\cos\theta_1\cos\theta_2$ $\times(\cos\theta_1+\cos\theta_2)$
14	$\lvert A_\parallel\rvert\lvert A_S\rvert$	$C\cos(\delta_{2,1}-\delta_S)$	$S\sin(\delta_{2,1}-\delta_S)$	$\cos(\delta_{2,1}-\delta_S)$	$D\sin(\delta_{2,1}-\delta_S)$	$\frac{4\sqrt{2}}{\sqrt{3}}\sin\theta_1\sin\theta_2$ $\times(\cos\theta_1+\cos\theta_2)\cos\Phi$
15	$\lvert A_\perp\rvert\lvert A_S\rvert$	$\sin(\delta_2-\delta_S)$	$-D\sin(\delta_2-\delta_S)$	$C\sin(\delta_2-\delta_S)$	$S\sin(\delta_2-\delta_S)$	$-\frac{4\sqrt{2}}{\sqrt{3}}\sin\theta_1\sin\theta_2$ $\times(\cos\theta_1+\cos\theta_2)\sin\Phi$

Table 3: Coefficients of the time-dependent terms and angular functions used in equation 37. Amplitudes are defined at $t=0$.

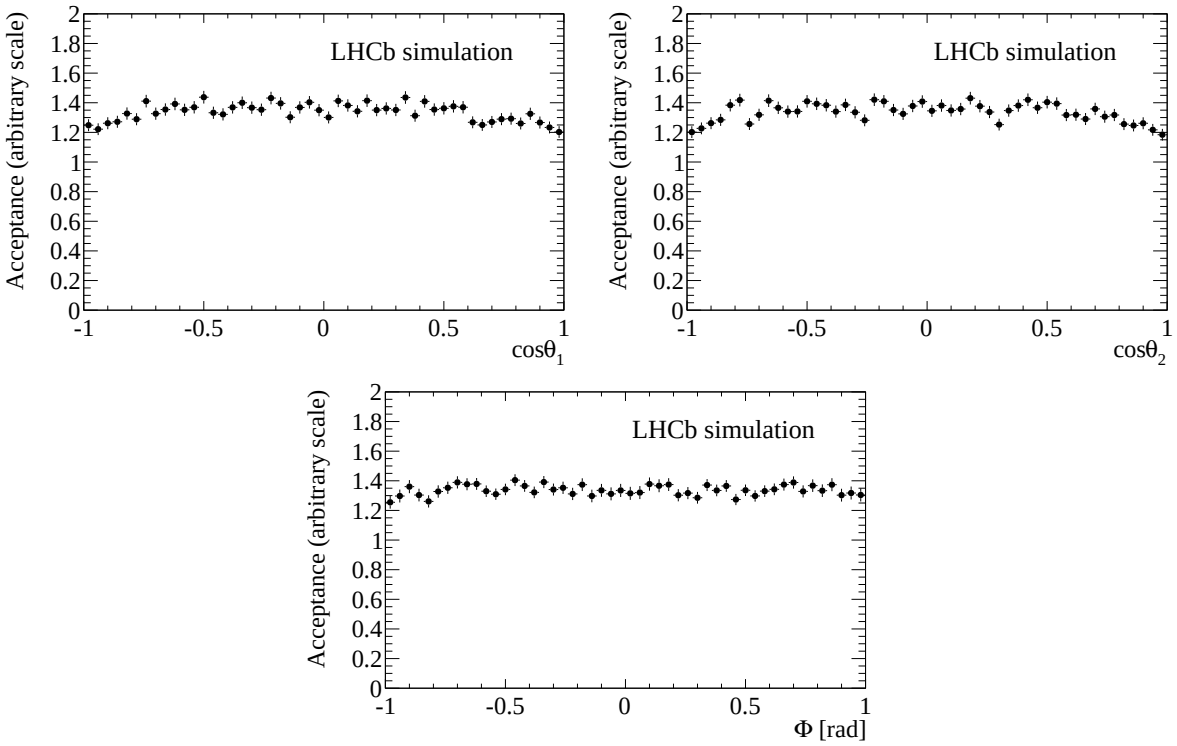

Figure 30: Acceptance corrections for each angle for the decay $B_s^0 \to \phi\phi$ from fully selected MC. Note that the scale is arbitrary.

the KK mass range is divided into two regions only, below and above the known ϕ mass. Having two ϕ mesons, this leads to 4 bins in 2 mass dimension as sketched in Fig. 31, where two bins are symmetric and joined as one bin.

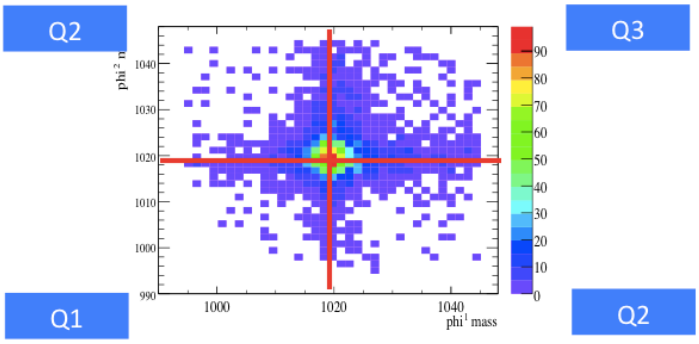

Figure 31: Difference between reconstructed decay time and the exact decay time of truth matched events from MC 2011(left) and MC 2012(right). Also plotted is the result of a double Gaussian fit.

The effect of using a finite m_{KK} range $[\mu_l, \mu_h]$ can be incorporated through making the substitutions

$$|A_i(\mu)|^2 \to \int_{\mu_l}^{\mu_h} |A_i(\mu)|^2 \mathrm{d}\mu \qquad \to \int_{\mu_l}^{\mu_h} |a_i g(\mu)|^2 \mathrm{d}\mu \quad \text{for } i \in \{\|, \perp, 0, S, SS\}. \tag{43}$$

For the P-wave component, the form of $g(\mu)$ is known to be a Breit-Wigner whereas for the S-wave component, the mass-dependence is assumed to be flat:

$$g_P(\mu) = \sqrt{\frac{\Gamma_\phi/2}{\Delta\lambda}} \cdot \frac{1}{\mu - \mu_\phi + i\Gamma_\phi/2}, \tag{44}$$

$$g_S(\mu) = \sqrt{\frac{1}{\Delta\mu}}. \tag{45}$$

With these functions, the effective coupling parameter C_{SP} is computed as

$$\int_{\mu_l}^{\mu_h} g^*(\mu) h(\mu) \mathrm{d}\mu \equiv C_{SP} e^{i\theta_{SP}}, \tag{46}$$

where the results are given in Table 4 for the whole ϕ mass region and when dividing into a lower and upper region. The larger C_{SP} factor allows a larger handle on the S-wave amplitudes with the disadvantage of having 3 independent amplitudes to be fit.

$m_{K^+K^-}$ Range	C_{SP}
$[994.455, 1044.455]$	0.36
$[994.455, 1019.455]$	0.69
$[1019.455, 1044.455]$	0.69

Table 4: Coupling factors between the S-wave and P-wave based on a flat S-wave model.

9 Fit procedure and results

9.1 Maximum Likelihood Fit

A probability density function (PDF) $\mathcal{P}(\vec{x}; \vec{a})$ describes the probability to measure certain variables $\vec{x}$ with given parameters $\vec{a}$. $\mathcal{P}(\vec{x}; \vec{a})$ is positive and the integral over the whole variable space $\int \mathcal{P}(\vec{x}; \vec{a}) d\vec{x} = 1$ since the probability to measure anything is one. However, $\mathcal{P}(\vec{x}; \vec{a})$ does not give the probability for a parameter set $\vec{a}$ given a measurement $\vec{x}$, but the probability to measure $\vec{x}$ given a parameter set $\vec{a}$, i.e. $\mathcal{P}(\vec{x}; \vec{a}) = \mathcal{P}(\vec{x}|\vec{a})$.
The likelihood function $\mathcal{L}$ is defined by the product of the single event probabilities of all events e:

$$\mathcal{L} = \prod_{e=1}^{N_{events}} \mathcal{P}(\vec{x}_e, \vec{a}), \tag{47}$$

where N_{events} is the total number of events. The best estimation of the parameter set $\vec{a}$ is obtained by maximizing the likelihood $\mathcal{L}$ to observe the given data set $\vec{x}$. Taking the negative logarithm of the likelihood function $\mathcal{L}$ facilitates the procedure and turns it into a minimization problem:

$$-ln\mathcal{L} = -\sum_{e=1}^{N_{events}} ln\mathcal{P}(\vec{x}_e;\vec{a}). \tag{48}$$

In this analysis, the measured variables are the reconstructed B_s^0 candidate decay time t, the helicity angles Φ, θ_1, θ_2 and the flavour tag q. The main parameters to fit are the CP-violating phase ϕ_s, the decay width Γ_s, $\Delta\Gamma_s$, Δm_s, the angular amplitudes A_i and the strong phase differences δ_j.

9.1.1 Gaussian constraints

Since the parameters Γ_s, $\Delta\Gamma_s$ and Δm_s have already been determined independently from this analysis, there is no reason not to profit from these measurements to constrain them in the fit. However, it is not desirable to fix them to constant values but to constrain them to their measured ones within the experimental uncertainties. This is done by adding an additional term to the negative logarithmic likelihood function $\mathcal{L}$:

$$-ln\mathcal{L} = -\sum_{e=1}^{N_{events}} \left\{ ln\mathcal{P}(\vec{x}_e;\vec{a}) + \sum_{i=1}^{N_{constraints}} \frac{(a_i - a_{i,meas})^2}{2\sigma_{i,meas}^2} \right\}, \tag{49}$$

where $N_{constraints}$ is the number of constrained parameters, $a_{i,meas}$ is the measured value of the i'th parameter and $\sigma_{i,meas}$ its experimental uncertainty. In this way, these parameters a_i are still included in the fit but the negative logarithmic likelihood increases quadratically with an increasing deviation from $a_{i,meas}$, which prevents it from drifting away.

9.2 Results

The decay time-dependent fit is implemented separately by the Edinburgh and Heidelberg groups. The data is split according to the four trigger categories and according to the invariant masses of the ϕ candidates. This is done separately for 2011 and 2012 data, with all datasets having been fitted simultaneously. The results of the fit to the parameters of interest are given in Table 5. The S-wave and double S-wave parameter estimations for the three regions are found to be consistent with zero as given in Table 6.

Cross-checks are performed on simulated datasets generated with the same number of events as observed in data, and with the same physics parameters, to ensure that generation values are recovered with negligible biases.

The scan of the natural logarithm of the likelihood for the ϕ_s parameter is shown in Fig. 32. At each point in the scan, all other parameters are re-minimised. A parabolic minimum is observed, and a point estimate provided. The shape of the profile log-likelihood is replicated in simplified simulations as a cross-check.

Table 5: Results of the decay time-dependent fit.

Parameter	Best fit value
ϕ_s (rad)	-0.17 ± 0.15
$\lvert A_\perp \rvert^2$	0.305 ± 0.013
$\lvert A_0 \rvert^2$	0.364 ± 0.012
δ_1 (rad)	0.13 ± 0.23
δ_2 (rad)	2.67 ± 0.23
Γ_s (ps^{-1})	0.662 ± 0.006
$\Delta\Gamma_s$ (ps^{-1})	0.102 ± 0.012
Δm_s (ps^{-1})	17.774 ± 0.024

Table 6: S-wave and double S-wave results of the decay time-dependent fit for the three regions, where M_{Q1} indicates the region with both two-kaon invariant masses smaller than the known ϕ mass, M_{Q2} the region with one smaller and one larger, and M_{Q3} indicates the region with both two-kaon invariant masses larger than the known ϕ mass.

Region	$\lvert A_S \rvert^2$	δ_S(rad)	$\lvert A_{SS} \rvert^2$	δ_{SS}(rad)
M_{Q1}	0.006 ± 0.012	-0.40 ± 0.53	0.009 ± 0.016	-2.99 ± 1.27
M_{Q2}	0.006 ± 0.010	2.76 ± 0.39	0.004 ± 0.011	-2.17 ± 0.72
M_{Q3}	0.001 ± 0.003	-2.58 ± 2.08	0.020 ± 0.022	0.53 ± 0.55

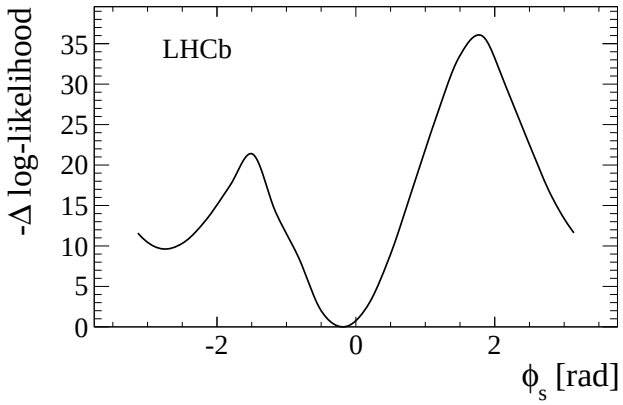

Figure 32: Profile log-likelihood for the ϕ_s parameter.

Figure 33 shows the distributions of the B_s^0 decay time and the three helicity angles. Superimposed are the projections of the fit result. The projections are event-weighted to yield the signal distribution and include acceptance effects.

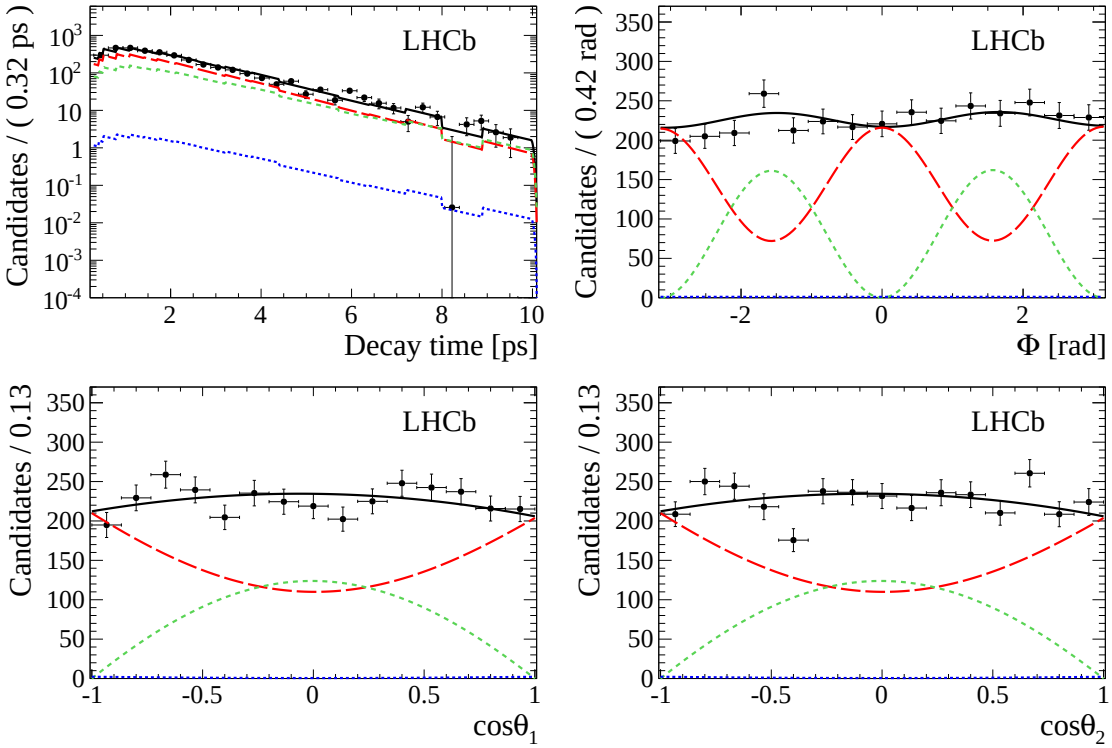

Figure 33: One-dimensional projections of the $B_s^0 \to \phi\phi$ fit for (top-left) decay time with binned acceptance, (top-right) helicity angle Φ and (bottom-left and bottom-right) cosine of the helicity angles θ_1 and θ_2. The background-subtracted data are marked as black points, while the black solid lines represent the projections of the best fit. The *CP*-even P-wave, the *CP*-odd P-wave and S-wave combined with double S-wave components are shown by the red long dashed, green short dashed and blue dotted lines, respectively.

9.2.1 Estimation of systematic uncertainties

A summary of the systematic uncertainties are given in Table 7. The dominating systematic uncertainties are due to the time acceptance and the angular acceptance. The uncertainty due to the decay time acceptance has been derived from the difference in the simulated decay time acceptances shown in Figure 25. In order to quantify the effect on the fitted parameters, toy studies have been performed with the same dataset size as used for the nominal result with the same fitted parameters measured in data, except for the CP-violating phase. Two thousand toy datasets have been generated for the value of ϕ_s as measured in the data with the decay time acceptance of simulated $B_s^0 \to \phi\phi$ events applied and fitted with the simulated $B_s^0 \to D_s\pi$ decay time acceptance, giving two thousand toy datasets in total. The average bias on each fitted parameter is then taken as the systematic uncertainty. The uncertainty due to the angular acceptance correction comes from the finite MC statistics and possible varying acceptances for the different trigger categories. The corrections are varied according to the errors and the deviation from the

best fit values is taken as the systematic uncertainty.

Parameter	Mass model	Angular acc.	Fit bias	Time acc.	Peak. BG	Total
$\|A_0\|^2$	–	0.007	–	0.005	–	0.009
$\|A_\perp\|^2$	–	0.004	–	0.003	–	0.005
δ_1 (rad)	0.03	0.02	0.02	0.02	0.01	0.05
δ_2 (rad)	0.04	0.02	–	0.05	0.01	0.07
ϕ_s (rad)	–	0.02	–	0.02	–	0.03

Table 7: Summary of systematic uncertainties for physics parameters in the decay time-dependent measurement.

10 Conclusion

With the 2011 and 2012 LHCb datasets of 3 fb^{-1} of integrated luminosity, no evidence for CP violation can be claimed in the channel $B_s^0 \to \phi\phi$. With approximately 4000 signal events, the measured value of the CP-violating phase ϕ_s of -0.17 $\pm$ 0.15 $\pm$ 0.03 is compatible with the SM expectation value. The uncertainties are statistically dominated and will decrease with the expected new data of 5 fb^{-1} in LHC Run II. Additionally, the upgraded LHCb detector of LHC Run III is expected to provide significantly improved reconstruction and trigger efficiencies which are especially beneficial for this four-hadronic final state. With the future LHCb data of 50 fb^{-1}, the precision of the ϕ_s measurement can become comparable to the theoretical uncertainties of 0.02.

References

[1] G. Hiller and U. Uwer, in *Physics at the Terascale, Chapter Quark Flavour Physics*, pp. 163–186, Wiley-VCH Verlag GmbH & Co. KGaA, 2011. doi: 10.1002/9783527634965.ch8.

[2] M. Neuner, *Measurement of the CP-violating phase ϕ_s in $B_s^0 \to J/\Psi\pi^+i^-$ decays at the lhcb experiment*, Diplomarbeit .

[3] (LHCb Collaboration), R. e. a. Aaij, *Search for CP violation in the decay $B_s^0 \to \phi\phi$ with the full LHCbRun I dataset*, LHCb-ANA-2014-035 (2014) .

[4] R. A. et al, *Measurement of the CP-violating phase in $B_s^0 \to J/\Psi\pi^+i^-$ decays*, Physics Letters B **736** (2014) 186 .

[5] (LHCb Collaboration), R. A. et al, *Precision measurement of CP violation in $B_s^0 \to J/\Psi K^+K^-$ decays*, Phys. Rev. Lett. **114** (2015) 041801.

[6] LHCb collaboration, A. A. Alves Jr. *et al.*, *The LHCb detector at the LHC*, JINST **3** (2008) S08005.

[7] L. Collaboration, *$Performance\ of\ the\ LHCb\ RICH\ Detector$*, Eur. Phys. J. C (2013) 73:2431 (2013) .

[8] (LHCb Collaboration), R. e. a. Aaij, *Measurement of CP violation in $B_s^0 \to \phi\phi$ decays*, Phys. Rev. D **90** (2014) 052011.

[9] M. Schmelling, *$LHCb\ Software\ \&\ Analysis\ Week:\ sWeights$*, 2014.